A Diagnostic Study of Recurrent Meteorological Anomalies Appearing in a 15-Year Simulation with a GFDL General Circulation Model

NGAR-CHEUNG LAU

Geophysical Fluid Dynamics Program, Princeton University, Princeton, NJ 08540

(Manuscript received 18 May 1981, in final form 3 August 1981)

ABSTRACT

The spatial structure and temporal characteristics of prominent anomalies occurring in a 15-year simulation with a GFDL spectral general circulation model are examined using empirical orthogonal functions, teleconnection patterns, composite charts, lagged correlation functions and frequency spectra.

Despite the absence of any nonseasonal perturbation in the prescribed forcing such as sea surface temperature, insolation and cloud cover, the simulated circulation exhibits an appreciable degree of temporal variability on monthly time scales. The standing oscillation in the Northern Hemisphere winter which accounts for the largest fraction of this variance has a coherent three-dimensional structure. In the middle and upper troposphere, this preferred mode of oscillation is characterized by a wavelike pattern with multiple centers of action. The corresponding anomaly pattern at the sea level is dominated by north–south pressure seesaws over the North Atlantic and North Pacific. The flow patterns associated with these pressure anomalies are consistent with the principal temperature anomaly pattern in the lower troposphere. The large-scale features of the above anomaly patterns are similar to those associated with the most prevalent standing oscillation observed in the atmosphere. The synoptic behavior and hydrological processes in the model atmosphere during the outstanding anomalous episodes are internally consistent.

The spatial structure of the principal mode in the simulation is rather insensitive to the averaging period of the model data. The autocorrelation function and frequency spectrum of the first principal component, as determined from daily data, are characteristic of persistent phenomena with no preferred periodicity. The autocorrelation time scale associated with this anomaly pattern is estimated to be ~15 days.

The principal anomaly pattern in the Northern Hemisphere summer is relatively less organized, while those for the Southern Hemisphere and the tropics are noted for their zonal symmetry. The east–west sea level pressure seesaw associated with the observed Southern Oscillation over the Pacific is not simulated by the model, thus suggesting the potential role of nonseasonal forcing mechanisms (such as sea surface temperature anomalies) in that phenomenon.

1. Introduction

Pursuant to the identification of well-defined oscillations in large-scale atmospheric circulation patterns by Walker and Bliss (1932), much effort has been devoted to document the spatial structure and frequency characteristics of meteorological anomalies occurring in different geographical regions. The growing body of observational evidence lends support to the existence of several spatially coherent and slowly-varying atmospheric fluctuations. The following sets of phenomena are particularly well-established:

- The North Atlantic Oscillation, in which the surface pressure tendency over the Icelandic Low is opposite to that over the subtropical North Atlantic. The anomalous flow pattern associated with this standing oscillation brings about extremities of wintertime temperature in that region (e.g., Walker and Bliss, 1932; Kutzbach, 1970; van Loon and Rogers, 1978).
- Standing pressure oscillations in the extratropical middle troposphere, characterized by preferred configurations of multiple "centers of action". These centers correspond to the regions where standing fluctuations attain maximum amplitudes. They are favorable sites for the prolonged occurrence of amplified ridges and troughs (Dickson and Namias, 1976; Wallace and Gutzler, 1981).
- The Southern Oscillation, in which the surface pressure tendency over Indonesia and Australia is opposite to that over the eastern South Pacific. This rearrangement of the mass field over the tropical belt is accompanied by systematic changes in precipitation, temperature and circulation in the zonal and meridional planes (e.g., Walker and Bliss, 1932; Kidson, 1975; Wright, 1977; Julian and Chervin, 1978).

Further investigations suggest interrelationships between the individual oscillatory phenomena mentioned above. Bjerknes (1969), Namias (1976) and Horel and Wallace (1981) have linked the Southern

0027-0644/81/112287-25$10.25

Oscillation to circulation features in extratropical latitudes. Wallace and Gutzler (1981) have demonstrated that the North Atlantic Oscillation at sea level tends to coexist with a large-scale 500 mb standing wave oscillation in the Pacific–North American sector. The observational evidence presented by Kutzbach (1970) and van Loon and Rogers (1978) indicates that the North Atlantic Oscillation is associated with a similar oscillation in surface pressure over the North Pacific.

In conjunction with our expanded empirical knowledge of long-term atmospheric variability, various hypotheses have been advanced to account for the dynamical and physical processes involved in the onset, maintenance and eventual breakdown of the observed circulation anomalies. Bjerknes (1966, 1969) and Namias (1969), among others, have proposed that localized sea surface temperature anomalies could play a significant role in the variability of the planetary-scale circulation. The steady-state response of the atmosphere to these and other perturbations in the external forcing was investigated by Webster (1972, 1981), Gill (1980), Opsteegh and van den Dool (1980), and Hoskins and Karoly (1981) using linear mechanistic models. In order to identify the influence of ocean surface temperature, control experiments with more complicated general circulation models (GCM's) have also been analyzed by Rowntree (1972, 1976a,b), Kutzbach *et al.* (1977), and Chervin *et al.* (1980).

Recently, an alternative view of the origin of circulation anomalies has been offered by Charney and DeVore (1979), who demonstrated that a multiplicity of solutions exists for an idealized channel model with fixed boundary forcing. They hence suggested that meteorological anomalies could be the manifestation of different equilibrium states for a given set of external forcing. In the light of this finding, atmospheric variability on monthly time scales could be caused by intermittent transitions from one equilibrium state to another. Such transitions could occur even in the absence of any perturbation to the external driving.

The nature of atmospheric variability has also been examined from the perspective of statistical sampling. Leith (1973) pointed out that the variance and autocovariance associated with daily weather fluctuations may account for a substantial portion of the interannual variability of finite-time (e.g., monthly or seasonal) averages. This notion was examined by Madden (1976) and Stefanick (1981) using observational weather records. As one examines the underlying causes for the variability of the atmospheric circulation on time scales of weeks and longer, it is hence necessary to take into account the residual noise associated with daily weather changes.

In the present study the variability of the atmospheric circulation in the course of a 15-year GCM integration is examined. This model experiment was conducted at the Geophysical Fluid Dynamics Laboratory (GFDL) by S. Manabe and his associates. The model used incorporates most of the essential physical and dynamical processes. However, such prescribed conditions as solar declination and sea-surface temperature were constrained to evolve through 15 identical annual cycles. The entire model integration proceeded with no nonseasonal changes in external parameters. The basic statistics of the model variability are presented in a companion paper by Manabe and Hahn (1981). The principal objective of the present paper is to diagnose the nature of the fluctuating phenomena in this "unperturbed" model atmosphere. In doing so we wish to gain some insight into the issues raised in the studies cited in the preceding paragraphs. In particular, we shall direct our attention to the following questions:

- Given the dynamical framework of the model and in the absence of any nonseasonal fluctuations in the imposed external forcing, are the observed modes of oscillation described earlier still identifiable in the model simulation?
- Do these persistent and spatially coherent anomaly patterns contribute significantly to the interannual variability of the model atmosphere? Or are the low-frequency fluctuations in the simulation entirely attributable to the residual noise associated with less organized daily weather disturbances?
- What is the synoptic behavior of the model during the outstanding anomalous episodes?

The data sets used in this study are described in Section 2. The analysis techniques are described in Section 3, which contains most of the terminology and notations used in this paper, and may be skipped by those readers who are already familiar with the usage of these diagnostic tools. A brief summary of various statistics of the 15-winter model climatology is given in Section 4. The spatial patterns of the principal model anomalies in the Northern Hemisphere winter are described in Section 5 using eigenvectors and teleconnection maps, and in Section 6 using composite charts. The temporal characteristics of these anomalies are examined in Section 7. A less detailed survey of the anomaly patterns for other regions and other seasons is presented in Section 8, followed by discussions in Section 9.

2. Data sets

a. Model data

The model data set consists of the global grids of selected variables sampled at daily intervals. The time series used were extracted from the model

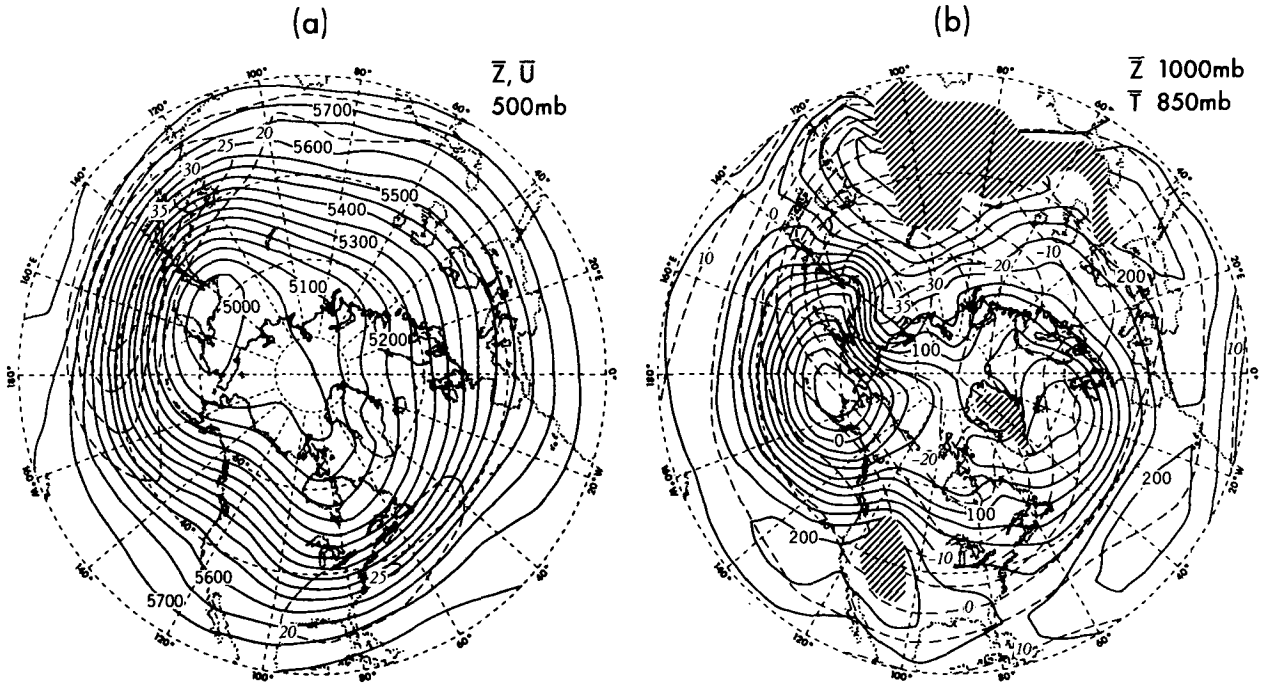

FIG. 1. Distributions of (a) geopotential height (solid contours, units: m) and zonal wind (dashed contours, units: m s^{-1}) at 500 mb; and (b) geopotential height at 1000 mb (solid contours, units: m) and temperature at 850 mb (dashed contours, units: °C); based on time averages over 15 simulated winters. The shaded areas in (b) indicate local topographic heights greater than 1500 m.

history tapes for the last 15 years of a 17.75-year simulation. The specifications of the GCM under investigation are described in detail by Gordon and Stern (1974), Manabe *et al.* (1979), and Manabe and Hahn (1981). Horizontal variations of the atmospheric variables are represented in terms of spherical harmonics with a rhomboidal truncation at 15 wavenumbers. Variations in the vertical direction are computed at nine levels in a sigma-coordinate system. Orography and ocean–continent contrast are incorporated into the lower boundary of the model. Of particular note is the fact that the prescribed annual cycles of insolation, sea surface temperature and ozone concentration do not vary from year to year.

b. Observational data

The observational data base consists of the monthly mean grids of 1000 and 500 mb heights, and 850 mb temperature, for the 15 winters (Dec–Jan–Feb) from 1962–63 to 1976–77. These analyses were produced by the U.S. National Meteorological Center (NMC) on an operational basis, and provide coverage of the region north of the 20°N latitude.

3. Analysis techniques

a. Bandpass filter

The behavior of synoptic-scale disturbances with time-scales of several days is examined by subjecting the time series of daily data to a 21-point bandpass filter described by Blackmon and Lau (1980). This filter retains those fluctuations with periods between 2.5 and 6 days.

b. Removal of the seasonal cycle

Except for the time-mean (Fig. 1) and bandpass filtered (Fig. 2) results, as well as for some of the composite charts, all analyses of the variability of monthly averaged, 5-day averaged and daily data are based on time series from which the normal seasonal cycle has been removed. This is accomplished by subtracting the 15-year average of each respective calendar day from the original time series to obtain deviations.

c. Scalar empirical orthogonal function

Empirical orthogonal functions or principal components offer an optimal and objective representation of the spatial and temporal variability of a meteorological field. This method is readily applicable to climatological analyses since the spatial features and time dependence of recurrent departures from normal can be depicted by a few patterns and indices, respectively. The approach adopted here essentially follows that outlined by Kutzbach (1967, 1970). In brief, given the $M \times N$ matrix $\mathsf{F}(x)$ for a scalar atmospheric variable x, with element $f_{m,n}(x)$ representing the departure from

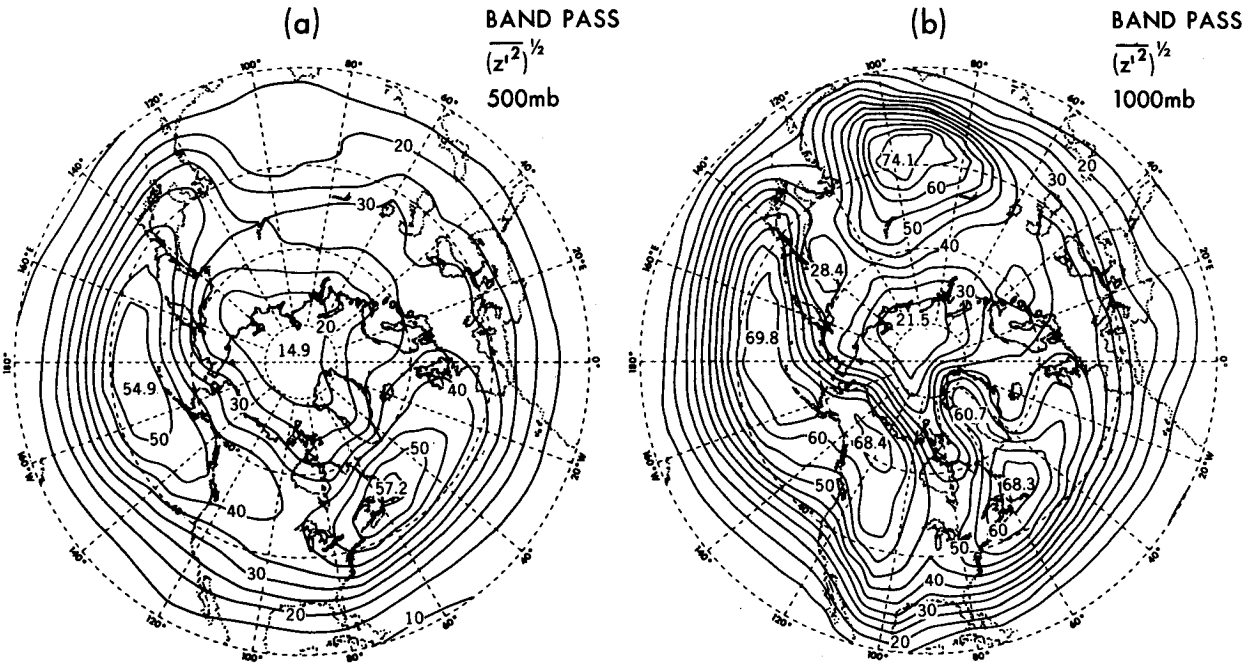

FIG. 2. Distributions of the rms of geopotential height at (a) 500 and (b) 1000 mb, based on bandpass filtered daily data for 15 simulated winters. Units: m.

normal of x at grid point m (m = 1 to M) in time n(n = 1 to N), one forms the $M \times M$ covariance matrix

$$\mathsf{R}(x) = \mathsf{F}(x)\mathsf{F}^{\mathrm{T}}(x)/N \qquad (1),$$

where the superscript T denotes the transpose. If all elements in $\mathsf{F}(x)$ were normalized by the local standard deviation, $R_{i,j}(x)$ would be the temporal correlation coefficient between fluctuations at grid point i and those at grid point j. The eigenvector associated with the kth principal component, denoted as $\mathbf{e}_k(x)$, is a column vector with M components satisfying the relation[1]

$$\mathsf{R}(x)\mathbf{e}_k(x) = \lambda_k(x)\mathbf{e}_k(x) \qquad (2),$$

where the magnitude of the eigenvalue $\lambda_k(x)$ represents the amount of variance explained by $\mathbf{e}_k(x)$, and provides a basis for ordering the eigenvectors according to their relative importance. This is achieved by arranging $\lambda_k(x)$ and $\mathbf{e}_k(x)$ such that $\lambda_1(x) > \lambda_2(x) > \lambda_3(x)$. . . . The eigenvectors are normalized such that $\mathbf{e}_k^{\mathrm{T}}(x)\mathbf{e}_k(x) = 1$. Each eigenvector describes a preferred mode of oscillation, and may be presented in the form of a contour map. The sites of maxima and minima in such a map indicate the centers of action of the corresponding mode. Each center of action in the eigenvector pattern is characterized by a given polarity (either plus or minus). The phase of the oscillation at those centers of the same polarity is opposite to the phase at the remaining centers of the other polarity.

The temporal evolution of the kth component is examined by considering the N-element coefficient vector

$$\mathbf{C}_k(x) = \mathbf{e}_k^{\mathrm{T}}(x)\mathsf{F}(x) \qquad (3),$$

with elements $C_{k,n}(x)$ representing the spatial correlation between the kth eigenvector and the pattern of x at time n. $\mathbf{C}_k(x)$ may be displayed in the form of a time series. Those months during which the anomaly pattern exhibits a strong spatial relationship with the kth eigenvector are signified by maxima or minima in this time series.

The methodology outlined above may be used to obtain a combined representation of the spatial and temporal variability of two or more atmospheric variables (see Kutzbach, 1967). In that case the input array F in (1) would include the data for all variables under investigation. For instance, if three variables x, y and z are used in the combined eigenvector representation, and if each of these variables is specified at M grid points and N time periods, $\mathsf{F}(x, y, z)$ would be a $3M \times N$ matrix. The elements $f_{m,n}$, $f_{M+m,n}$ and $f_{2M+m,n}$ in this matrix represent the departure from normal of x, y, z, respectively, at grid point m in time n. The corresponding covariance or correlation coefficient matrix $\mathsf{R}(x, y, z)$ would have dimensions $3M \times 3M$ [see (1)]. The eigenvectors $\mathbf{e}_k(x, y, z)$ associated with $\mathsf{R}(x, y, z)$ would have $3M$ elements and may be presented in three

[1] The solutions to this eigenvalue equation were obtained using the computer subroutines EIGSFM (for the scalar case) and EIGHFS (for the complex case) described in NCAR (1978).

separate contour maps. Each of these maps has M grid points and depicts the spatial pattern for one of the three variables. The temporal variation of this combined representation is similarly described by the N-element coefficient vector $\mathbf{C}_k(x, y, z)$ [see Eq. (3)].

d. Complex empirical orthogonal function

The formulation developed in the previous subsection may be generalized to analyze the anomaly pattern of vector variables (Hardy and Walton, 1978). In the case of the vector field of horizontal wind (V), the input data to the matrix F(V) are complex numbers with real and imaginary parts corresponding to the zonal and meridional wind components, respectively. The elements of the eigenvectors $\mathbf{e}_k(\mathbf{V})$ are complex and may be presented as arrows on a chart. The elements of the coefficient vectors $\mathbf{C}_k(\mathbf{V})$ are in general also complex. In order to allow for meaningful physical interpretation, the imaginary part of the time series of coefficients is minimized by rotating every complex element in $\mathbf{e}_k(\mathbf{V})$ through a constant angle, which is determined for each individual principal component by the slope of a least-square-fit to the N elements in $\mathbf{C}_k(\mathbf{V})$ (see Hardy and Walton, 1978).

e. Teleconnection pattern

The spatial structure of prevalent anomaly patterns may be described alternatively by mapping the temporal correlation coefficients between the fluctuations at a fixed reference location and the simultaneous values at other sites in the domain of interest. Such a pattern is referred to as a 1-point teleconnection map. It corresponds to one of the rows (or columns) of the matrix $\mathsf{R}(x)$ in (1), if the input data $\mathsf{F}(x)$ were normalized by the local standard deviation of x. The appropriate reference locations [or, the appropriate rows of $\mathsf{R}(x)$] for the construction of these patterns may be identified by a systematic inspection of all possible teleconnection maps (Wallace and Gutzler, 1981), or by considering the centers of action showing up in the dominant eigenvectors of $\mathsf{R}(x)$.

4. Northern Hemisphere wintertime circulation statistics

The presentation of the 15-winter model climatology is confined to a few parameters. Blackmon and Lau (1980, hereafter referred to as BL) have performed a more extensive analysis of the simulation of a single winter by a grid-point GCM developed earlier at GFDL. They have noted the problems associated with inadequate sampling of slowly varying fluctuations when one compares a single-season simulation with long term observational records. It is anticipated that the increased sample size offered by the present 15-year simulation should provide for a more reliable assessment of the fidelity of the model climatology.

a. Time-mean fields

In Fig. 1 are shown the hemispheric distributions of (a) 500 mb height and zonal wind, and (b) 1000 mb height and 850 mb temperature, averaged over 15 winter seasons (Dec–Jan–Feb). The time-mean circulation at 500 mb in both the observed (Blackmon, 1976, Fig. 3b; Blackmon *et al.*, 1977, Fig. 6a) and modeled (Fig. 1a) atmospheres is characterized by prominent pressure troughs and intensified zonal flows over the east coasts of the Asian and North American land masses. The presence of a third trough over eastern Europe is also simulated. The observed pressure ridge over Bering Strait is displaced eastward in the model result, and the simulated trough over eastern Asia is seen to extend too far into the central Pacific.

As is noted by Manabe and Hahn (1981), the location of most of the major pressure centers near the sea level (Fig. 1b) is simulated by the model. However, the Aleutian Low in the model is too intense and is displaced north of its observed position by about 5° of latitude. It is also seen that the geostrophic flow over North America is much too zonal. Such differences between model simulation and observations are also discernible in the results presented in BL. The simulated 850 mb temperature over northeastern Siberia is lower than the observed values (BL, Fig. 15a). Also evident in Fig. 1b is the prevalence in the lower troposphere of warm advection over the western and central portions of the Eurasian and North American land masses, and cold advection over the eastern seaboards of these continents.

b. Geopotential height fluctuations

In Fig. 2 are shown the distributions of the root-mean-squares (rms) of geopotential height $(\overline{z'^2})^{1/2}$ at (a) 500 and (b) 1000 mb, based on the bandpass filtered (see Section 3a) time series for the 15-winter simulation. Here the overbar denotes a time average and the prime denotes a deviation from time average. The elongated axes of maximum in these patterns correspond to the principal cyclone tracks, where synoptic-scale disturbances are particularly active. Both observed (BL, Fig. 8a) and simulated (Fig. 2a) storm tracks in the middle troposphere are located downwind of the mean wintertime jet streams and extend across the Pacific and Atlantic along the 45–50°N zone. The simulated bandpass fluctuations over these centers of activity are characterized by strong poleward and upward heat transports in the lower troposphere, and by strong flux convergence

of westerly momentum near the tropopause (not shown).

The locations of the simulated oceanic storm tracks at 1000 mb (Fig. 2b) agree with observations (BL, Fig. 11a). Both observed and simulated patterns suggest the existence of two distinct cyclone tracks in the North Atlantic sector. One of these tracks is directed across the ocean toward the British Isles; the other extends northward from Newfoundland and reaches the western shores of Greenland. The amplitude of the 1000 mb fluctuations in the model is generally higher than the observed result. There are indications of enhanced disturbances on the leeward side of the Rockies and the Himalayas. However, the model maxima in variability over the northwestern portions of Canada and China are not evident in the observed result, nor do they show up in the corresponding pattern for another model simulation with no orography (not shown). These unrealistic features are probably caused by too intense lee-slope cyclone development in the model, and by the necessity for data extrapolations below the ground surface in regions of high terrain.

As a measure of simulated month-to-month variability in the middle troposphere, the rms field of monthly averaged 500 mb height is shown in Fig. 3. This pattern is based on data for 45 winter months in the 15-year integration, and may be compared with the corresponding observed result, shown in Blackmon *et al.* (1979, Fig. 1b). Both observed and modeled atmospheres are characterized by enhanced intermonthly variability over the Pacific and Atlantic. Contrary to the observed distribution, the model result gives two separate maxima in the North Atlantic sector. The third region of activity north of Siberia in the observed pattern is displaced eastward by about 60° of longitude in the simulated pattern. The rms amplitude of the monthly means of the model data is ~70–80% of that observed in the atmosphere.

The geographical variations in the vertical structure of geopotential height fluctuations in the model may be inferred from Fig. 4, which shows the distributions of (a) the temporal correlation coefficient between the 500 and 1000 mb heights, and (b) the ratio between the standard deviations of the 500 and 1000 mb heights. These model results are based on monthly averaged data for 15 winters. The strong positive correlations over the central and eastern oceans in the middle latitudes (Fig. 4a) are indicative of the equivalent barotropic nature of the fluctuations in these regions. The relatively lower or negative correlations over the interiors of the North American and Eurasian land masses reflect the presence of much more baroclinic fluctuations over these areas. With the exception of the local minimum near the Kamchatka Peninsula, as well as the much too high values over northwestern Canada, the large-scale features in Fig. 4a correspond well with those in the observed pattern (Blackmon *et al.*, 1979, Fig. 2).

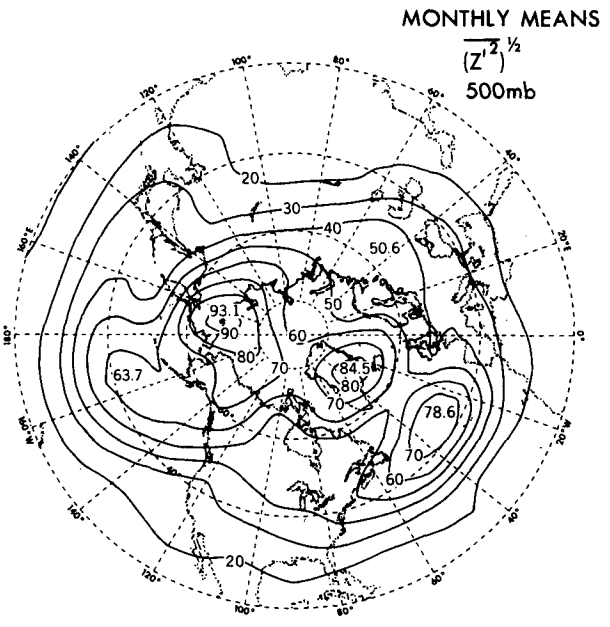

FIG. 3. Distribution of the rms of geopotential height at 500 mb, based on monthly means for 15 simulated winters. Units: m.

The amplitudes of the monthly mean geopotential height fluctuations at 500 mb are comparable to those at 1000 mb over much of the eastern oceans (Fig. 4b). The ratio between the amplitudes at these levels increases westward and peaks over the southeastern seaboards of Asia and North America. These regional variations are also evident in the observed pattern (Blackmon *et al.*, 1979, Fig. 4).

Maps analogous to those shown in Fig. 4 have been drawn on the basis of daily, 5-day averaged and seasonally averaged data. The large-scale aspects of the resulting patterns (not shown) are similar to those derived from monthly means (Fig. 4). This lack of frequency dependence of the vertical anomaly structure is in agreement with the observational findings reported by Blackmon *et al.* (1979).

5. Eigenvectors and teleconnection maps for Northern Hemisphere winter

All model results presented in this section are based on monthly averages for 15 simulated winters (Dec–Jan–Feb). The input data for all variables were normalized by the respective local standard deviation. For 500 and 1000 mb heights, the eigenvector analysis (see Section 3c) was performed on the 112-point grid depicted by solid dots in Fig. 5a. For 850 mb temperature, data for those grid points corresponding to regions of high terrain (depicted

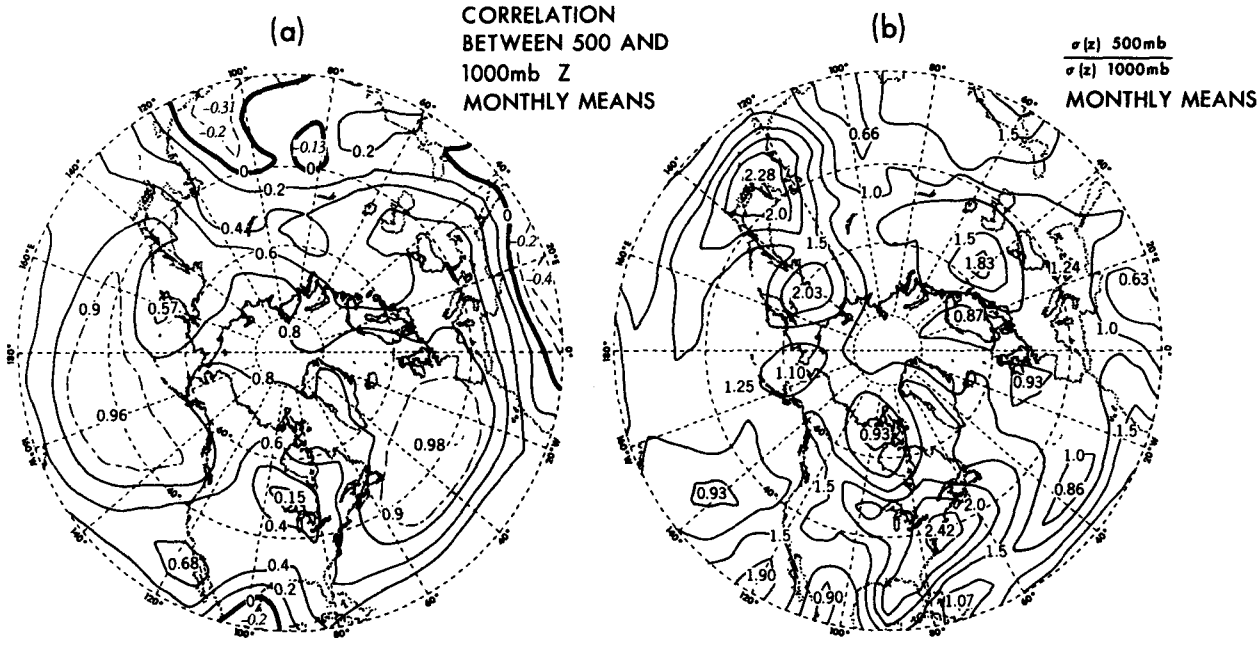

FIG. 4. (a): Distribution of correlation coefficient between simulated monthly averaged 500 and 1000 mb heights during winter. (b): Distribution of the ratio of standard deviation of 500 mb height to that of 1000 mb height, based on simulated monthly averages for winter.

by open circles in Fig. 9a) were not included in the analysis. The complex eigenvector analysis for the 200 mb horizontal motion (Section 3d) was performed on a grid consisting of 248 points located at the centers of the arrows shown in Fig. 11. The percentages of domain-integrated variance explained by the first three principal components for different variables presented in this study, along with other pertinent particulars, are summarized in Table 1.

The present discussion is confined to the first principal components. For the model data, the eigenvectors presented here were determined individually for each atmospheric variable. The observed eigenvectors used for comparing with the model results were based on monthly mean NMC analyses (Section 2b). These observed patterns are associated with the first principal component of a combined eigenvector representation (see Section 3c and Kutzbach, 1967) of 500 mb height, 850 mb temperature and 1000 mb height. A detailed discussion of the rationale and procedures for using the three-variable representation in analyzing the observed data is given in the Appendix.

a. 500 mb height

In Fig. 5 are shown the distributions of the first eigenvector for 500 mb height, based on (a) model data and (b) observations (see Appendix). A teleconnection pattern (see Section 3e) for model data with reference point at 34°N, 165°W[2] is displayed in Fig. 6. This particular reference point (depicted by a solid dot in Fig. 6) is selected for its proximity to one of the centers of maximum amplitude (or centers of action) in the first eigenvector based on model data (Fig. 5a). Teleconnection charts based on other centers of action (e.g., those at 74°N, 180°W; 29°N, 128°E or 38°N, 45°W) in Fig. 5a (not shown) are characterized by essentially the same pattern as Fig. 6.

The high spatial correlation between Figs. 5a and 6 may be readily understood in terms of (1) and (2). For a given principal component k, if the reference point j is chosen such the jth element of $\mathbf{e}_k(x)$ is a local maximum or minimum (or, equivalently, if j corresponds to one of the centers of action in the kth eigenvector pattern), then by (2), the absolute value of the jth element of $\mathbf{R}(x)\mathbf{e}_k(x)$ would be maximized. Since the latter quantity is a measure of the spatial correlation between the teleconnection map with reference point j [i.e., the jth row of $\mathbf{R}(x)$] and the kth eigenvector [$\mathbf{e}_k(x)$], we would expect a strong resemblance between those two patterns. The maximization is most effective for the first few eigenvectors, since $\lambda_k(x)$ on the right-hand side of (2) is also large.

There are altogether five major centers of action in the model pattern for $\mathbf{e}_1(z)$ at 500 mb (Fig. 5a), which

[2] For the sake of brevity, all latitudes and longitudes referred to in this paper have been corrected to the nearest degree.

TABLE 1. Summary of specifications for the eigenvectors examined in the present paper. The fractions of domain-integrated variance explained by the first three eigenvectors in each individual principal component analysis are expressed in percent. The eigenvector analyses are all based on model data normalized by the local standard deviation.

Variable	Geopotential height (z)										Temperature (T)	Horizontal wind (V)
Level (mb)	1000				500					300	850	200
No. grid points	112			240	112					240	101	248
Domain	20–74°N			43°S–38°N	20–74°N				20–74°S	43°S–38°N	20–74°N	29°S–79°N
Season	DJF			All 12 months	DJF			JJA	JJA	All 12 months	DJF	DJF
Averaging period	1 month	5 days	1 day	1 month	1 month	5 days	1 day	1 month	1 month	1 month	1 month	1 month
Fig. no.	7a	—	—	24b	5a	—	—	25	26	24a	9a	11
Explained variance (percent)												
e_1	23.1	11.9	7.5	16.7	22.4	12.4	8.8	9.8	23.1	13.4	14.1	10.0
e_2	7.5	5.6	4.1	6.2	9.0	6.8	5.4	9.3	10.5	5.2	8.8	6.4
e_3	7.2	5.2	3.9	4.9	7.6	6.0	4.5	7.3	8.0	3.7	7.2	5.9

explains 22.4% of the hemispherically integrated variance (Table 1). Those months in the model simulation with strong positive coefficients [see Eq. (3)] for the first principal component are characterized by amplified troughs over the East China Sea, the central Pacific near the 170°W meridian, and the region extending from the eastern United States to southern Europe; and by amplified ridges over Greenland and regions adjoining the Bering Strait. By comparing Fig. 3 with Fig. 5a, it is seen that these anomaly centers correspond closely to regions of maximum variability in 500 mb height. Based on geostrophic considerations, the distribution of the height anomalies in Fig. 5a is associated with above normal westerly flow over the Pacific and Atlantic at about 30°N latitude, and above normal easterly flow at 40–60°N in the same sectors. Over the eastern Pacific between 140 and 160°W, the meridional flow in the months with large positive coefficients for the first eigenvector acquires a more southerly component than in the 15-winter mean. Conversely, the features noted above appear with the opposite polarity in those months with strong negative coefficients for this principal component.

There exists a spatial correspondence between the essential model features in Fig. 5a with those in the observed pattern (Fig. 5b). However, differences between simulated and observed patterns with re-

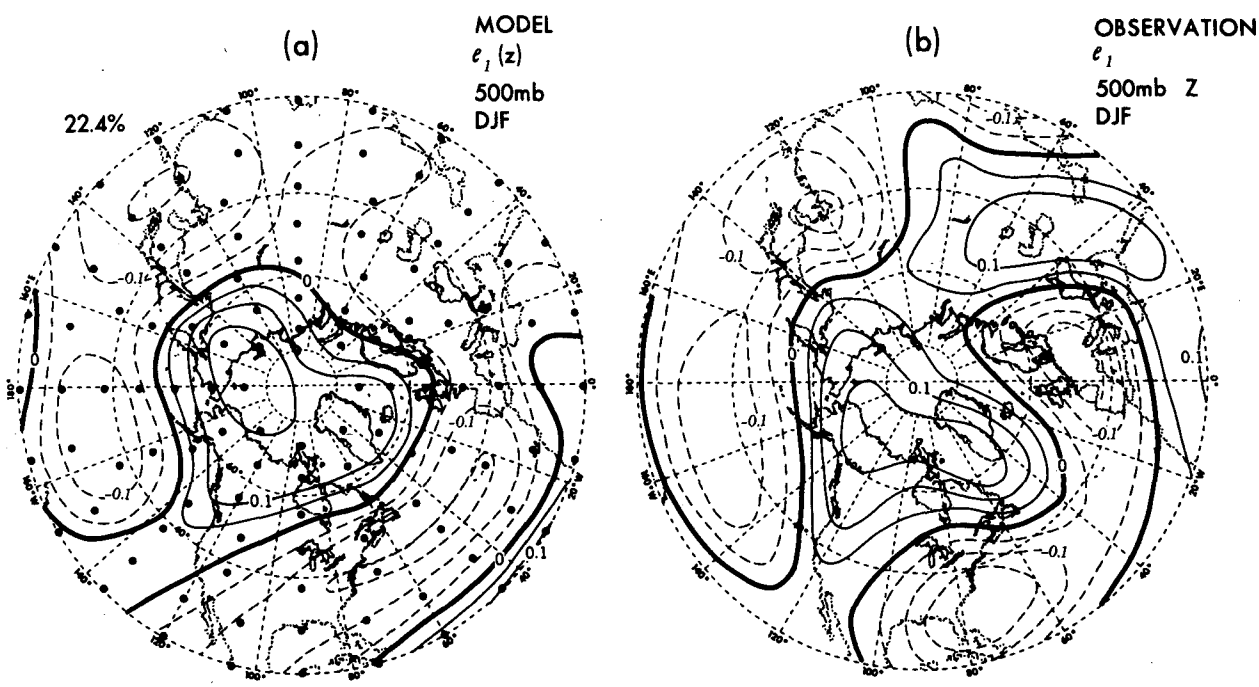

FIG. 5. Distributions of the first eigenvectors of normalized monthly mean 500 mb height field for winter, for (a) model and (b) observations (see Appendix). The solid dots in (a) indicate the grid points used in the eigenvector analysis.

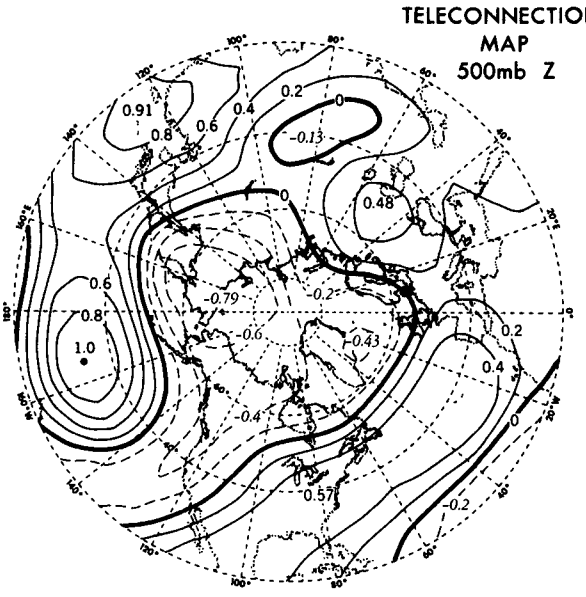

FIG. 6. Teleconnection map with reference point at 34°N, 165°W, based on model data for monthly mean wintertime 500 mb height.

spect to the exact location of the anomaly centers are discernible. The observed center over northern Canada is displaced toward the Arctic region in the model result. The model anomaly appearing over the midlatitude Atlantic is split into two centers in the observed pattern, with one located over the southeastern United States and the other over Europe. There is little evidence in the model simulation of the observed center over the Caspian Sea.

In comparing the model eigenvectors with observations, one should take into consideration the reproducibility of the principal components derived from data records of finite duration. Wallace and Gutzler (1981) have demonstrated that the observed eigenvectors for two separate groups of winters exhibit noticeable differences. Nevertheless, it is seen that the observed anomaly pattern shown in Fig. 5b of the present paper resembles one of the leading eigenvectors for both groups of winters (Wallace and Gutzler, 1981, Figs. 27b and 29a). Determination of the extent to which the model eigenvector (Fig. 5a) is reproducible would have to await the completion of even longer model integrations.

The teleconnection map (Fig. 6) bears some resemblance to the observed Pacific/North American pattern discussed by Dickson and Namias (1976, Figs. 2 and 3) and Wallace and Gutzler (1981, Fig. 16), and the composite charts presented by O'Connor (1969, p. 30) based on the occurrence of negative 700 mb 5-day mean anomalies at 40°N, 170°W. However, the simulated anomalies over the midlatitude Pacific are shifted slightly south of their observed positions, and the anomaly center noted by Wallace and Gutzler over northwestern Canada is less distinct in the model result.

A similar analysis has been performed using monthly mean model data at 300 mb. The results (not shown) are basically the same as those presented above. The eigenvector presented in Fig. 5a is found to be insensitive to the spatial domain of analysis, since experimentation with an expanded

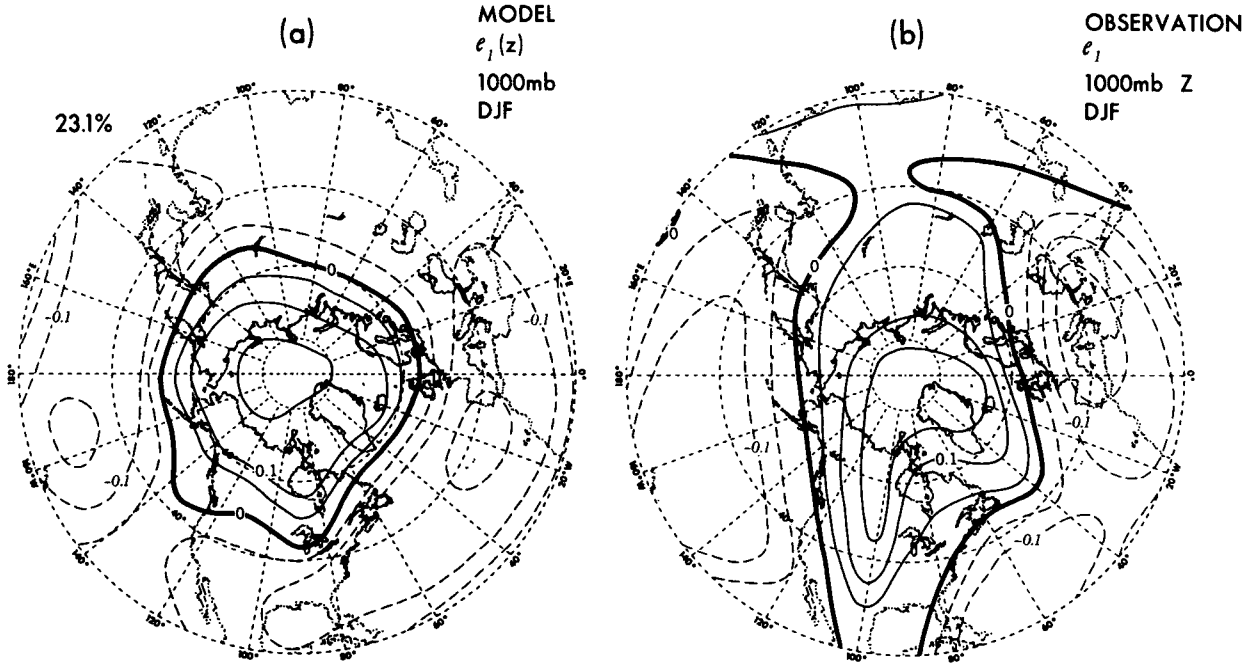

FIG. 7. As in Fig. 5, except for normalized monthly mean 1000 mb height field in winter.

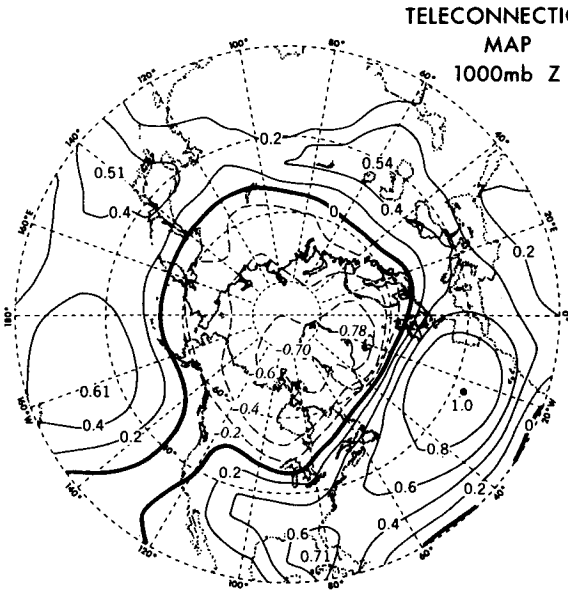

FIG. 8. Teleconnection map with reference point at 38°N, 23°W, based on model data for monthly mean wintertime 1000 mb height.

grid covering the entire Northern Hemisphere yields essentially the same result. The choice between normalized and unnormalized data does not influence the essential characteristics of that eigenvector, except that analysis of unnormalized data tends to deemphasize features in the subtropics, where the temporal variance is relatively low.

b. 1000 mb height

In Fig. 7 are shown the patterns of the first eigenvector for 1000 mb height, based on (a) model data and (b) NMC observational analyses for the winter season. The teleconnection map for model data with reference point at 38°N, 23°W (which corresponds to the center of action over central Atlantic in the first eigenvector of the model simulation) is presented in Fig. 8. The observed north–south pressure seesaw over the North Atlantic and the North Pacific (Fig. 7b) is evident in the corresponding model result (Fig. 7a). The observed pattern is more zonally asymmetric as a result of the following additional features:

- The observed pressure anomaly centered over the Arctic is associated with equatorward extensions along the 100°W, 40°W and 80°E meridians.
- The subtropical Atlantic anomaly in the observed pattern is split into two separate centers, with one located off the eastern seaboard of North America, and the other over the Mediterranean.

The teleconnection map associated with the first eigenvector of the model (Fig. 8) may be compared with observational results presented by Walker and Bliss (1932, Fig. 2), van Loon and Rogers (1978, Fig. 11) and Wallace and Gutzler (1981, Fig. 8). The zero contour over the Pacific (Atlantic) in the simulated pattern is seen to be located south (north) of the observed position.

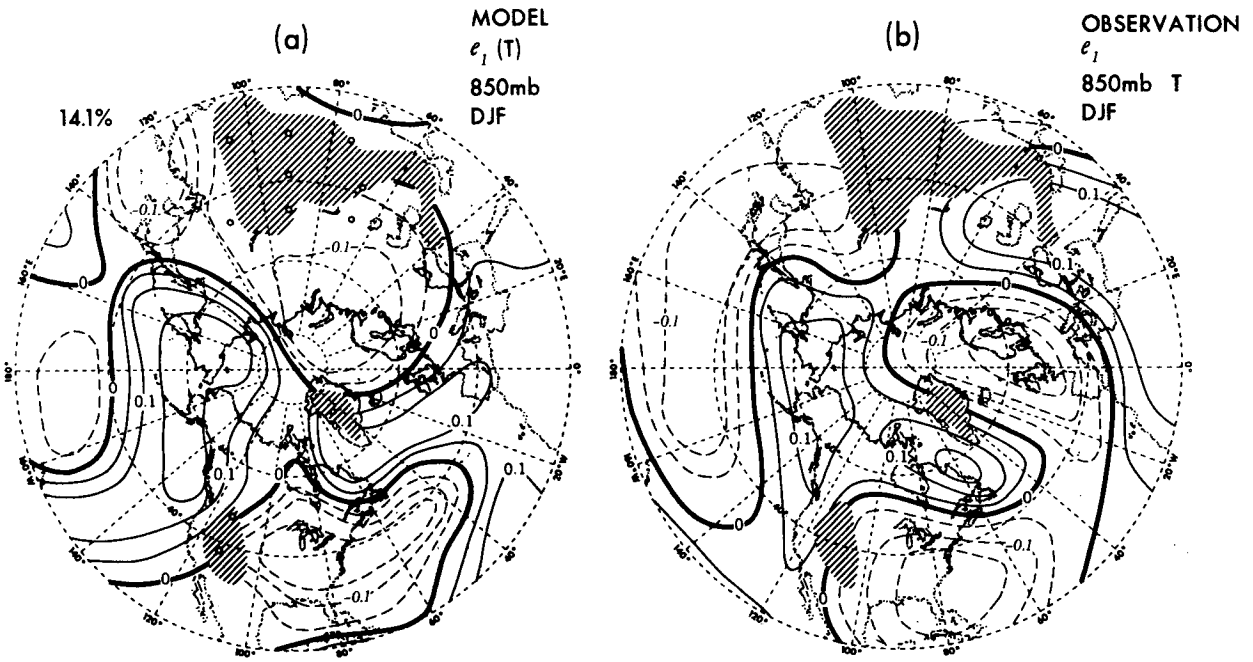

FIG. 9. As in Fig. 5 except for normalized monthly mean 850 mb temperature field in winter. The shaded areas indicate local topographic heights greater than 1500 m. The open circles indicate those grid points which are not used in the eigenvector analysis.

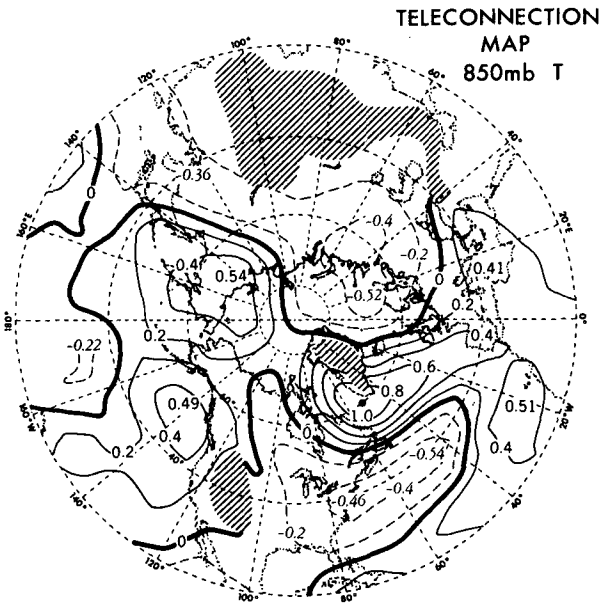

FIG. 10. Teleconnection map with reference point at 61°N, 53°W, based on model data for monthly mean wintertime 850 mb temperature.

c. 850 mb temperature

The first eigenvector of the temperature field at 850 mb is displayed in Fig. 9, for (a) the model and (b) observations. The teleconnection chart associated with the model eigenvector (with reference point at 61°N, 53°W) is shown in Fig. 10. Those winter months in the model simulation with positive coefficients for $\mathbf{e}_1(T)$ are characterized by cold anomalies over northern and eastern Europe, eastern United States and the surrounding waters, the subtropical Pacific between the 160°E and 160°W meridians, and the East China Sea; and by warm anomalies over western Greenland and the North Atlantic, southern Europe and the eastern subtropical Atlantic, and a broad region extending from the Kamchatka Peninsula to western North America and eastern subtropical Pacific. Most of these model features are supported by the observed eigenvector shown in Fig. 9b, and by the composite charts presented by van Loon and Rogers (1978, Fig. 9) based on those Januaries when the observed surface temperature anomalies over western Greenland and northern Europe are strong and of opposite sign. In the European sector, there are slight displacements of the simulated anomaly centers relative to the observed positions.

d. 200 mb horizontal wind

The anomalous circulation features over the tropics associated with the first eigenvector of 500 mb height (Fig. 5a) is discerned by performing a complex eigenvector analysis (see Section 3d) on the monthly mean horizontal vector wind field. The domain of analysis extends from 29°S to 79°N. The arrows in Fig. 11 represent the eigenvector for the first principal component of the simulated horizontal motion field at 200 mb during the Northern Hemisphere winter. Superimposed on the same pattern are contours of $\mathbf{e}_1(z)$ at 500 mb (Fig. 5a), which is almost identical to the corresponding result based on upper tropospheric data. In the middle and higher latitudes, the arrows exhibit a strong tendency to be aligned with the contours. In particular, the locations of the cyclonic vortices over the two ocean basins coincide with the negative centers of action in $\mathbf{e}_1(z)$ at 500 mb. The arrows further indicate the presence of two additional (anticyclonic) vortices over the subtropical Atlantic and Pacific, which are centered at the sites marked by *A* and *B*, respectively. The anomalous 200 mb airflow in the equatorial belt extending westward from the Atlantic

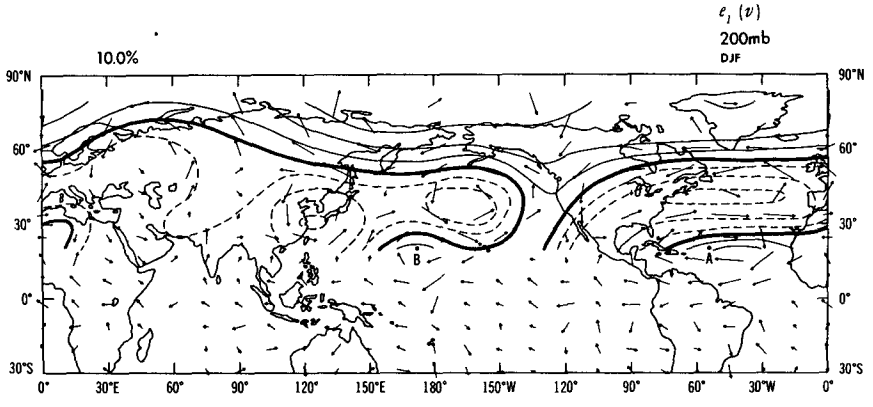

FIG. 11. Distribution of the eigenvector (arrows) associated with the first principal component of normalized monthly mean 200 mb horizontal wind during Northern Hemisphere winter. The first eigenvector of 500 mb height (contours, see Fig. 5a) is reproduced here for comparison. The labels *A* and *B* indicate the subtropical vortex centers discussed in the text. Arrows which are too short to show up clearly are not plotted.

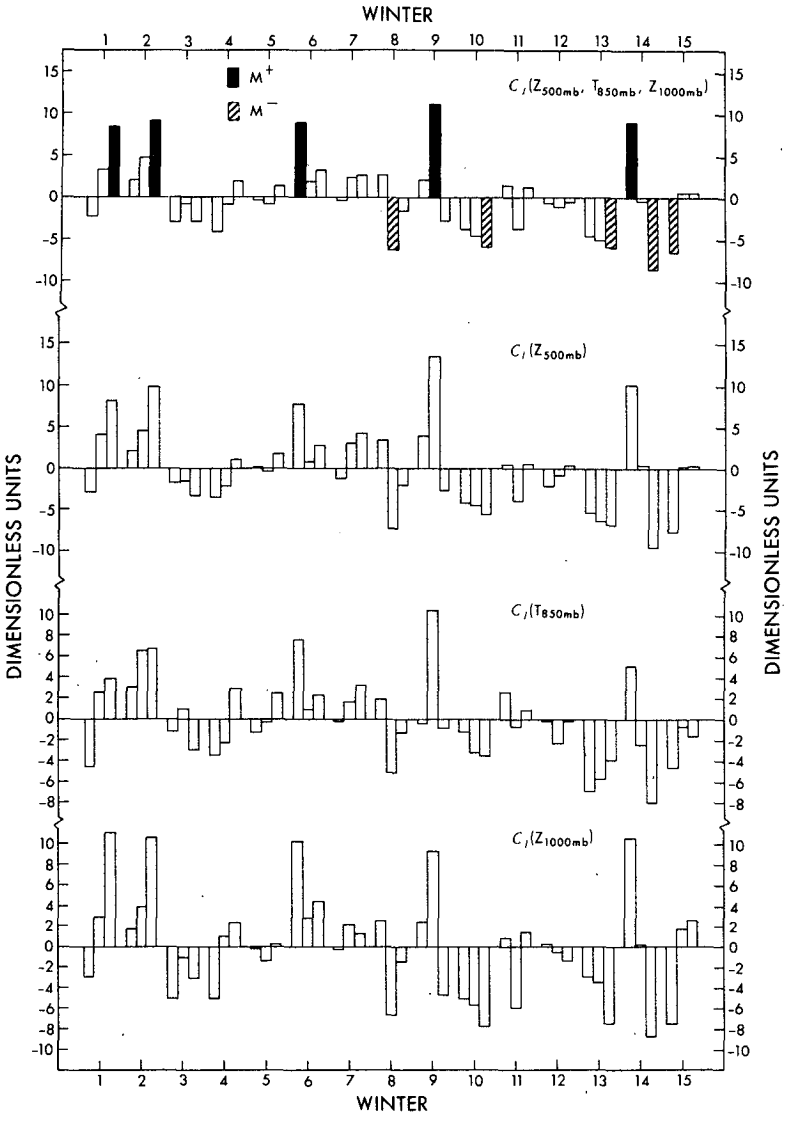

FIG. 12. Time series of the coefficients associated with the first principal component of 500 mb height, 850 mb temperature and 1000 mb height, as determined by a combined three-variable eigenvector representation (top panel) and by single-variable representations (bottom three panels). The input model data are monthly averages for winter (Dec–Jan–Feb). The solid (striped) columns in the series for $\mathbf{C}_1(z_{500}, T_{850}, z_{1000})$ indicate the five winter months with the highest positive (negative) coefficients.

to the Indonesian Archipelago is predominantly easterly for those months with large positive coefficients for the first principal component. There is little evidence of any spatially coherent features in $\mathbf{e}_1(\mathrm{V})$ south of the equator.

6. Composite charts of outstanding anomalous episodes

An eigenvector analysis of the monthly averaged model data for 500 mb height, 850 mb temperature and 1000 mb height was also performed using a combined three-variable representation (see Section 3c, and Kutzbach, 1967). The first eigenvector as determined using this method [$\mathbf{e}_1(z_{500}, T_{850}, z_{1000})$,[3] not shown] accounts for 19.1% of the total variance, and bears a strong resemblance to the corresponding patterns obtained by single-variable representations, shown in Figs. 5a, 7a and 9a. The spatial correlation coefficients between the first eigenvector patterns determined by the two methods are 0.997 for 500 mb height, 0.976 for 850 mb temperature, and 0.995 for 1000 mb height. The first eigenvectors presented in the previous section for individual fields

[3] The suffices indicate the pressure level.

TABLE 2. Temporal correlation coefficients between the time series displayed in Fig. 12, based on monthly mean wintertime data.

	$C_1(z_{500})$	$C_1(T_{850})$	$C_1(z_{1000})$
$C_1(z_{500}, T_{850}, z_{1000})$	0.99	0.93	0.98
$C_1(z_{500})$		0.92	0.94
$C_1(T_{850})$			0.84

hence describe different aspects of the same circulation anomaly having a coherent three-dimensional structure.

The relationship between the first model eigenvectors presented in Section 5 is further substantiated by the strong temporal correlations between the coefficients [see Eq. (3)] associated with these eigenvectors. The time series of these coefficients, shown in Fig. 12, are determined by a combined three-variable representation [$C_1(z_{500}, T_{850}, z_{1000})$, top panel] and by single-variable representations [$C_1(z_{500})$, $C_1(T_{850})$, $C_1(z_{1000})$, bottom three panels]. The temporal correlation coefficients between different pairs of time series are presented in Table 2. All values given here are found to be statistically significant at the 0.5% level by Student's t-test.[4]

[4] Noting the considerable autocorrelation inherent in the individual time series, we have made the conservative assumption that fluctuations within a given winter yield only one independent piece of information. Hence, taking 15 as the sample size, correlation coefficients > 0.64 can be regarded as significant at the 0.5% level.

In order to provide for a phenomenological description of the simulated circulation patterns corresponding to the outstanding anomalous episodes, two separate groups of model data are studied in this section. The first group consists of averages over those 5 months with the highest (most positive) coefficients associated with $e_1(z_{500}, T_{850}, z_{1000})$. These months are depicted by solid columns in Fig. 12, and are hereafter collectively referred to as M^+. The corresponding composite chart for variable x is denoted as $H(x)$. The other group is compiled by compositing those five months with the lowest (most negative) coefficients for the same principal component, and is denoted as $L(x)$. The latter months are depicted by columns with strips in Fig. 12, and are hereafter referred to as M^-.

In most cases the patterns obtained by subtracting the climatological mean separately from $H(x)$ and from $L(x)$ are similar to each other except for a reversal in sign. Hence it is sometimes sufficient to discuss the nature of the anomaly in terms of the pattern $H(x) - L(x)$.

a. Geopotential height and horizontal motion

In Fig. 13 are shown the composite patterns of geopotential height (solid contours) and zonal wind (dashed contours) at 500 mb, for months (a) M^+ and (b) M^-. $H(z)$ at 500 mb (Fig. 13a) is characterized by broad pressure troughs extending longitudinally from Japan and from the eastern United States far into the neighboring oceans. The pressure ridge over

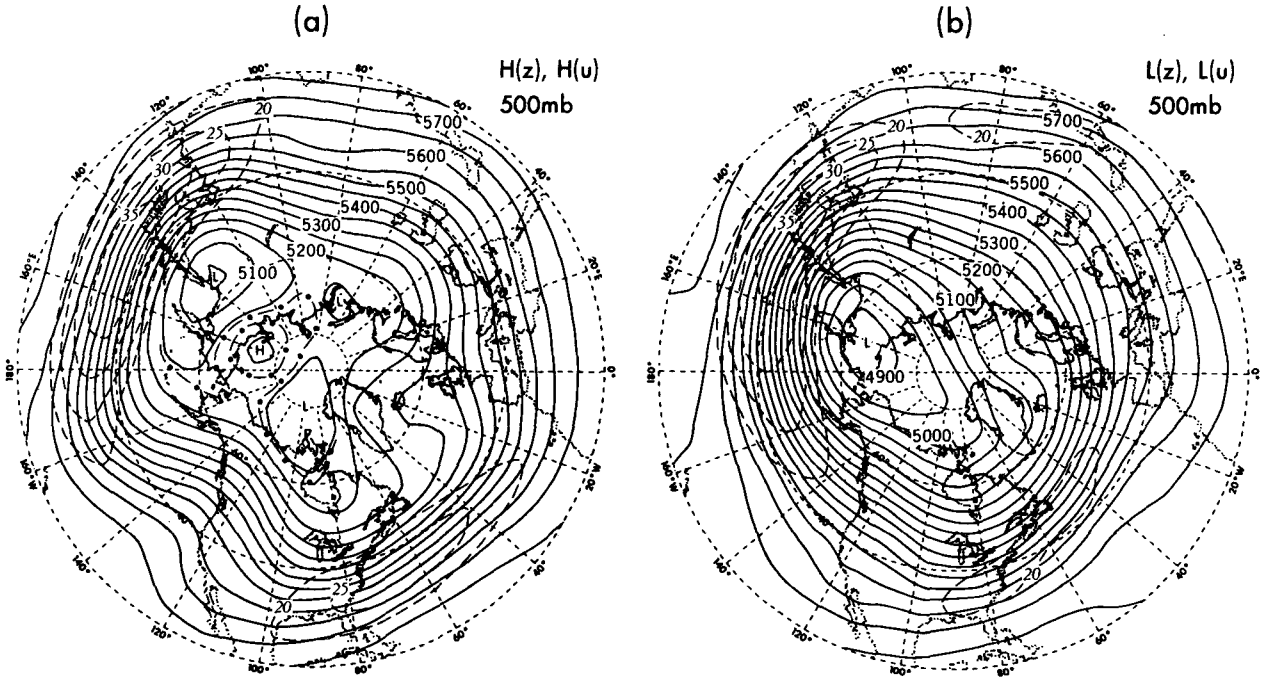

FIG. 13. Composite charts of simulated geopotential height (solid contours, units: m) and zonal wind (dashed contours, units: m) at 500 mb, based on five winter months (a) M^+ and (b) M^- (see text and Fig. 12). The lines with alternating dots and dashes in (a) are the 5160 and 5180 m height contours.

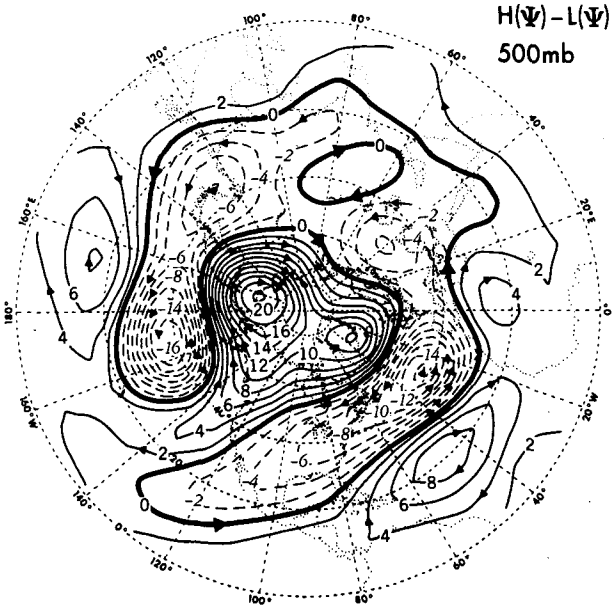

FIG. 14. Distribution obtained by subtracting the composite anomaly chart of simulated 500 mb streamfunction based on the five winter months M^- (see text and Fig. 12) from the corresponding anomaly chart based on the months M^+. Units: 10^6 m^2 s^{-1}. Note that the outermost circle in this map represents the equator.

western North America is amplified and extends toward the East Siberia Sea, resulting in above normal easterly flow over northeastern Siberia. The ridge over the northeastern Atlantic is also more prominent than normal and acquires an omega-shaped pattern. On the other extreme, $L(z)$ (Fig. 13b) is noted for the absence of amplified ridges over western Canada and Greenland, and for a relatively sharper trough over Japan. Comparison between $H(u)$ (Fig. 13a) and $L(u)$ (Fig. 13b) indicates a southward shift of the jetstream axes over the eastern oceans in the former pattern by as much as 10° of latitude. The intensity at the core of the North American jet appearing in $H(u)$ is stronger by ~5 m s^{-1} at 500 mb.

The horizontal flow field associated with the height anomalies described above is investigated by examining the streamfunction field ψ. In Fig. 14 is shown the 500 mb distribution of $H(\psi) - L(\psi)$ over the entire Northern Hemisphere (note that the domain of analysis is extended to the equator in this particular chart). The locations of the major vortices in this figure agree with those inferred from the patterns of $\mathbf{e}_1(z_{500})$ (Fig. 5a) and $\mathbf{e}_1(\mathbf{V}_{200})$ (Fig. 11). The occurrence of anomalous westerly flows over the oceans between the 20 and 40°N latitudes, and of anomalous easterly flow further north, is associated with the meridional displacements of the jet stream axes relative to their climatological positions (see Figs. 13a and 13b). The pattern in Fig. 14 illustrates more clearly the preferred southwest-to-northeast tilts of the elongated streamflow anomalies. These features are particularly evident in the North American and Atlantic sectors, where the vortices appear in juxtaposition with alternating signs. There is no indication of any spatially coherent feature near the equator.

The composite patterns for 1000 mb height are displayed in Fig. 15, for (a) $H(z)$, (b) $L(z)$ and (c) $H(z) - L(z)$. The Aleutian and North Atlantic Lows

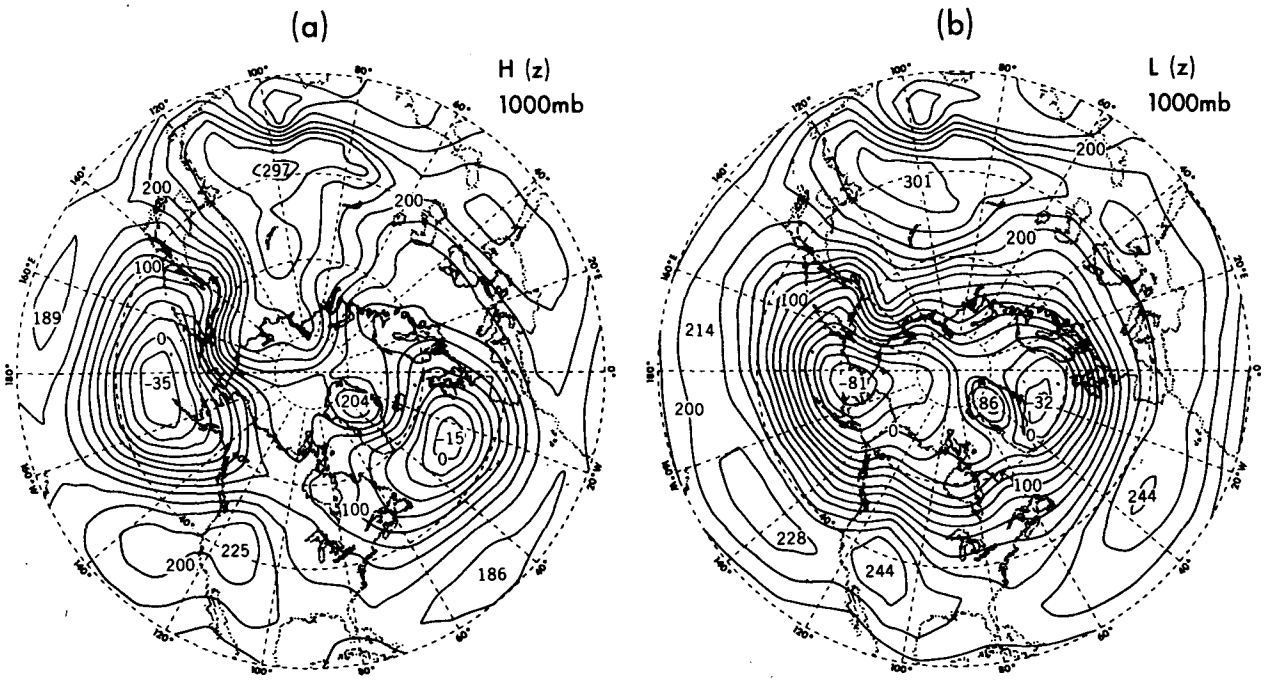

FIG. 15a and 15b. As in Figs. 13a and 13b except for composite charts of 1000 mb height. Units: m.

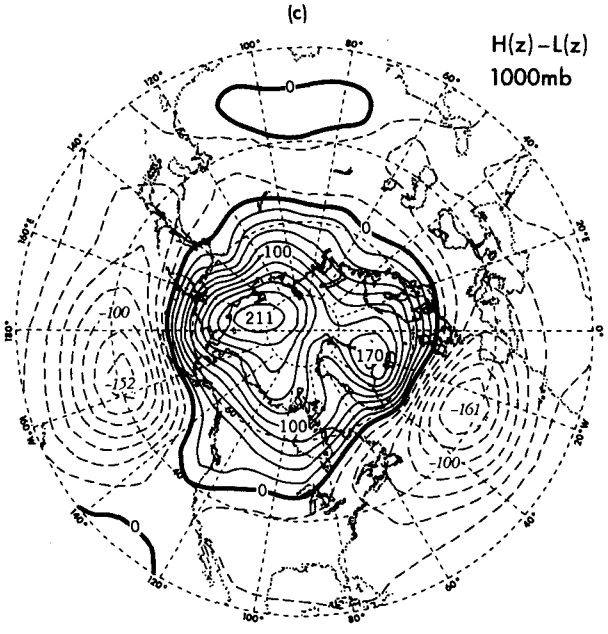

FIG. 15c. As in Fig. 14 except for composite anomaly charts of 1000 mb height. Units: m.

in $H(z)$ are located about 10° latitude south of their mean positions (cf. Fig. 15a and Fig. 1b). Associated with this configuration of low-pressure centers is the above-normal southerly surface flow over western Canada, above-normal northerly flow over eastern Canada, and above-normal sea level pressure over northern Greenland. The broad belt of westerlies across the North American continent in the long-term mean pattern (Fig. 1b) is much less evident in $H(z)$. The corresponding chart for $L(z)$ (Fig. 15b) is characterized by much deepened oceanic lows centered near the Arctic Circle. In the same months (M^-), the high-pressure cells over the subtropical Atlantic and subtropical Pacific are larger and more intense. These height changes result in above-normal westerly flow in the oceanic sectors between 50 and 60°N. The above features are more clearly seen in the distribution of $H(z) - L(z)$ at 1000 mb (Fig. 15c), which resembles that of $\mathbf{e}_1(z_{1000})$ (Fig. 7a). The extrema in Fig. 15 are also coincident with centers of maximum variability in 1000 mb height, as shown in Manabe and Hahn (1981, Fig. 5.3).

Comparison between the patterns of $H(z) - L(z)$ at 1000 mb (Fig. 15c) and at 500 mb (not shown, qualitatively similar to Fig. 14), as well as between $\mathbf{e}_1(z_{500})$ and $\mathbf{e}_1(z_{1000})$ (Figs. 5a and 7a), indicates that the major 500 and 1000 mb anomalies are centered at essentially the same geographical locations. This result is consistent with the strong temporal correlations between monthly averaged 500 and 1000 mb heights at the sites of these anomalies (Fig. 4a).

The nature of the simulated surface pressure patterns presented above is generally consistent with the synoptic description given by Kutzbach (1970, Section 4) pertaining to the first eigenvector of observed sea level pressure. However, the tendency for the depths of the observed Aleutian and Icelandic Lows to vary in opposition to each other (Kutzbach, 1970; van Loon and Rogers, 1978, Fig. 2; Wallace and Gutzler, 1981, Fig. 18) is not apparent in the present model simulation.

b. *Temperature and snowfall*

The contours in Fig. 16 show the distribution of $H(T) - L(T)$ for temperature at 850 mb. Superposed on the same pattern are shaded areas depicting maxima and minima in $H(S) - L(S)$ for snowfall rate S. The pattern of $H(T) - L(T)$ resembles that of $\mathbf{e}_1(T_{850})$ (Fig. 9a), and that of the teleconnection pattern associated with the observed temperature seesaw between northern Europe and Greenland (van Loon and Rogers, 1978, Fig. 9). Comparison between Figs. 15c and 16 indicates that the cold anomalies over eastern North America, northern and eastern Europe, East China Sea and subtropical central Pacific are under the influence of stronger than normal northerly flows in the lower troposphere. Conversely, anomalous southerly flows prevail over Greenland and regions around the northern Pacific when the temperature over these locations is above normal. Over the western Atlantic, the increase in baroclinicity along the 30–40°N belt is consistent with the intensification and southward displacement

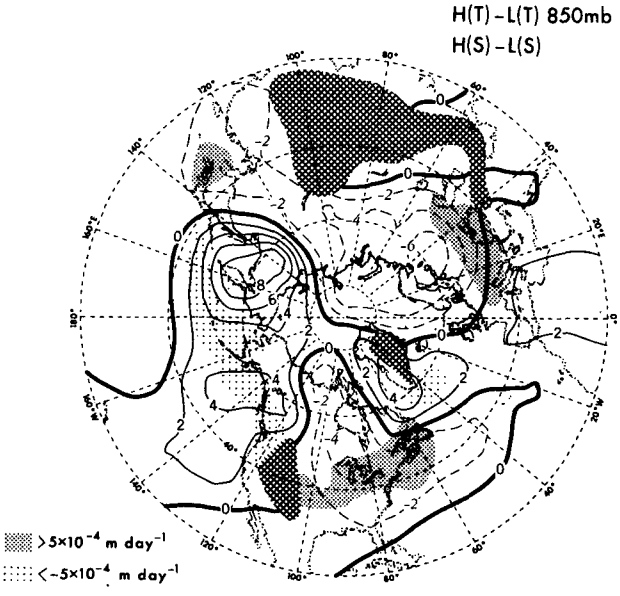

FIG. 16. As in Fig. 14, except for composite anomaly charts of 850 mb temperature (contours, units: °C), and of snowfall rate expressed in equivalent amount of water content (areas with heavy shading indicate values larger than 5×10^{-4} m day^{-1}; areas with light shading indicate values smaller than -5×10^{-4} m day^{-1}, features with absolute amplitude less than one standard deviation are omitted). Regions with local topographic heights greater than 1500 m are cross-hatched.

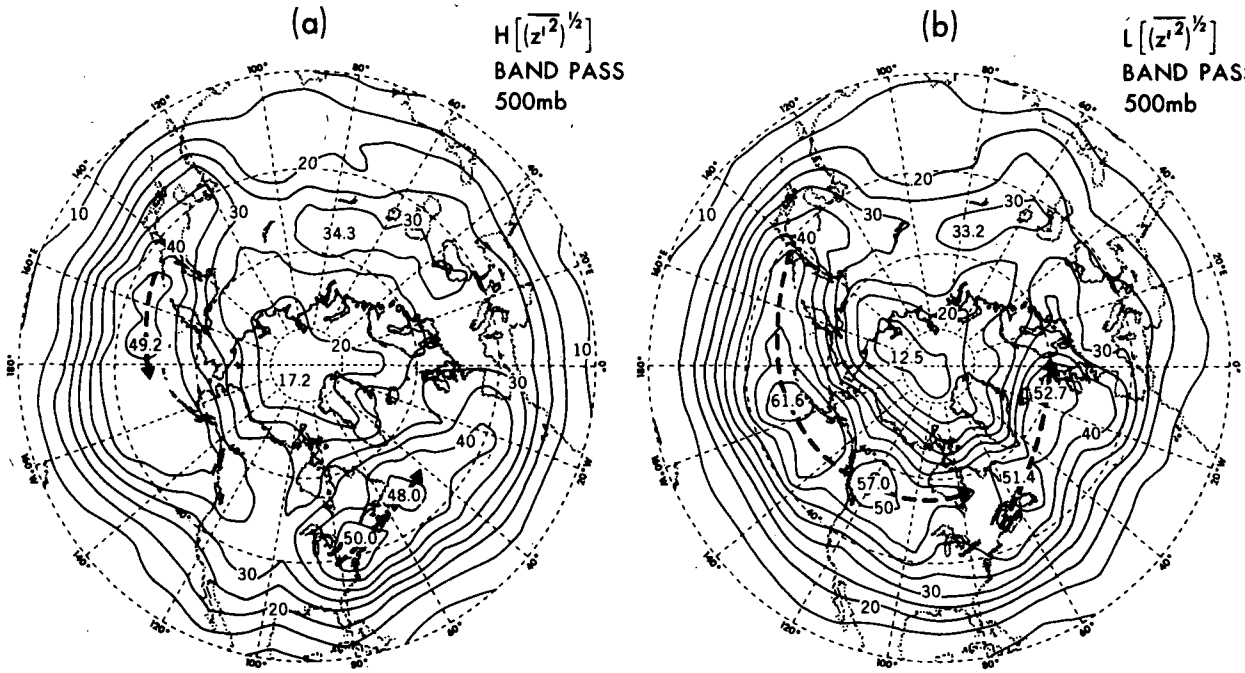

FIG. 17. As in Fig. 13, except for composite charts of rms of bandpass filtered 500 mb height. Units: m. The arrows with dashed shafts indicate those regions where the root-mean-squares are larger than 45 m.

of the North American jetstream in the pattern of $H(u)$ (Fig. 13a). The cold anomalies are generally associated with increased snowfall rates, and *vice versa*.

c. Cyclone tracks

In order to examine the behavior of cyclone-scale phenomena associated with the first principal component, composite charts of the rms geopotential height fields $(\overline{z'^2})^{1/2}$ are constructed using bandpass filtered (see Section 3a) time series for the anomalous months M^+ and M^-. The elongated maxima in these charts correspond to sites of enhanced variability with periods of several days, and are hence useful indicators of the position of the major storm tracks. In Fig. 17 are shown the patterns of (a) $H[(\overline{z'^2})^{1/2}]$ and (b) $L[(\overline{z'^2})^{1/2}]$ at 500 mb. Contrasting these two patterns, one notes that the disturbances along the cyclone tracks (depicted by arrows with dashed shafts) in months M^+ tend to diminish in strength well before they reach the west coasts of North America and Europe. It is seen that the Atlantic storm track is shifted more equatorward in months M^+. This meridional displacement of the storm track axis is seen to go hand in hand with a corresponding shift in the jetstream and baroclinic zone over the Atlantic (Figs. 13 and 16). The passage of cyclones across the eastern oceans in months M^+ (Fig. 17a) is evidently being blocked by the contemporary amplification of pressure ridges in these regions (Fig. 13a). Similar features are discernible in the corresponding maps for 1000 mb (not shown). These surface patterns further indicate that the surface storm track extending from Newfoundland across the Davis Strait to Greenland (see Fig. 2b) tends to be better established during months M^+.

On the basis of observed weather records for the period 1948–74, Dickson and Namias (1976, Figs. 7 and 8) have associated similar redistributions of North Atlantic storms over the southeastern United States with changes in the local baroclinicity. The relationship between the location of the cyclone track and jetstream axis has also been noted by Blackmon *et al.* (1977, Section 7).

d. Evaporation and precipitation

The variations in evaporation (E) and precipitation (P) rates associated with the anomalous months are illustrated by the composite charts in Fig. 18, for (a) $H(E) - L(E)$, and (b) $H(P) - L(P)$. The central Pacific between 20 and 40°N as well as the waters just off the southeastern seaboards of Asia and North America are characterized by above-normal evaporation during the months M^+. Below-normal evaporation prevails over the northern Atlantic and Pacific during the same months. The changes in evaporation rate over land from months M^+ to months M^- are much weaker than the corresponding changes over the oceans. A negative correlation exists between the maritime features in $H(T) - L(T)$ at 850 mb (Fig. 16) and those in $H(E) - L(E)$ (Fig. 18a). This relationship may be

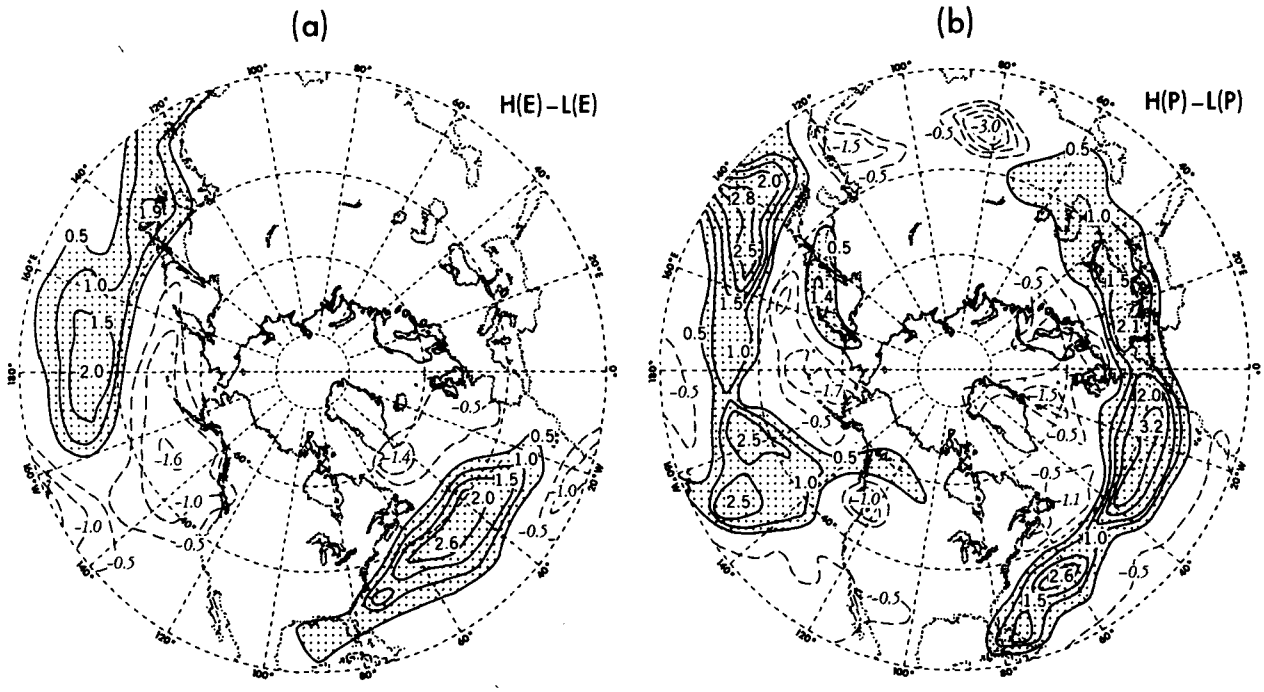

FIG. 18. As in Fig. 14 except for composite anomaly charts of (a) evaporation and (b) precipitation rates. Units: 1×10^{-3} m day^{-1}. For the sake of clarity, the zero contour is not plotted.

understood in terms of the parameterization scheme for evaporation adopted in the model [Manabe, 1969, Eq. (15)]. Over the ocean surface, evaporation is assumed to be directly proportional to the difference between the saturation mixing ratio of water vapor prescribed at the lower boundary and the actual mixing ratio at the lowest prognostic level. Evaporation is locally enhanced when cold and dry air masses originating from the Arctic or the interior of continents are brought into contact with the relatively warm waters off the east coasts of China and the United States. These cold-air outbreaks over the eastern seaboards are more frequent during the months M^+, since the attendent surface flow in these regions acquires a more northerly component (Fig. 15a). Conversely, the moist subtropical air masses accompanying the prevalent southerly flow tend to suppress evaporation over the northern oceans during the same months.

The most salient features in the composite pattern for precipitation rate $H(P) - L(P)$ (Fig. 18b) are the elongated bands of positive values spanning across the Pacific and the Atlantic along the 30–40°N zone. The feature over the Atlantic extends further eastward and has a secondary maximum over southern Europe. These two bands of enhanced precipitation during months M^+ coincide with the sites of below-normal sea level pressure (Fig. 15c). The above normal evaporation rates in the western portion of these bands (Fig. 18a) probably also contribute to an

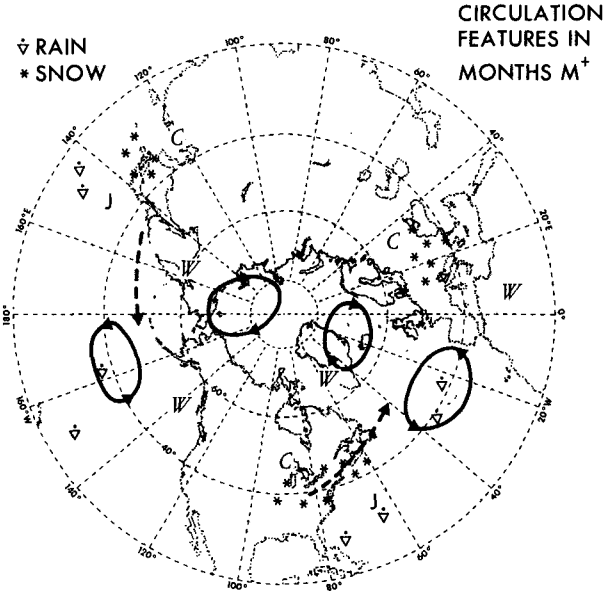

FIG. 19. Schematic diagram depicting the anomalous circulation features in months M^+. The shaded belt in high latitudes is bounded by the 5160 and 5210 m height contours in the pattern for $H(z_{500})$ (Fig. 13a). The shaded belt in middle latitudes in bounded by the 5550 and 5600 m height contours in $H(z_{500})$. The closed loops represent the anomaly centers of the 1000 mb height field (Fig. 15c). The cold and warm anomalies are identified by the letters C and W, respectively. Locations of the 500 mb storm tracks are indicated by arrows with dashed shafts. The jet stream cores are denoted by J. Above-normal snowfall and precipitation are indicated by an asterisk and $\dot{\nabla}$, respectively.

increased supply of moisture to these regions. Below-normal precipitation prevails over the northern Atlantic and Pacific, as well as northern Europe, which are characterized by above-normal sea level pressure during months M^+.

Rogers and van Loon (1979, Fig. 5) have composited observed precipitation data based on those Januaries when the temperature over Greenland is above normal and the temperature over northern Europe is below normal. These Januaries are analogous to the months M^+ considered here (see Fig. 16). Their result also indicates that such Januaries are associated with above-normal precipitation over the Azores and southern Europe, and by below-normal precipitation over Iceland.

e. Summary

The interrelationships between different synoptic phenomena occurring in months M^+ are summarized in Fig. 19. The shape of the circumpolar vortex at 500 mb, as determined from the pattern of $H(z)$ at 500 mb (Fig. 13a), is depicted by the shaded belts in this figure. The position and sign of the sea level pressure anomalies [i.e., $H(z) - L(z)$ at 1000 mb, see Fig. 15c] are indicated by closed loops. Regions with above and below normal temperatures in months M^+ (Fig. 1b) are identified by the letters W and C, respectively. The position and longitudinal extent of the principal cyclone tracks $H\{(\overline{z'^2})^{1/2}\}$, see Fig. 17a] are indicated by bold arrows with dashed shafts. Locations with enhanced snowfall (Fig. 16) and precipitation (Fig. 18) are denoted by the appropriate plotting codes used in conventional synoptic charts.

7. Temporal characteristics of the first eigenvector

Eigenvectors of the 500 and 1000 mb heights during winter (1 December to 28 February) were also determined using non-overlapping 5-day averages and daily data. The normal seasonal cycle has been removed from the time series of these shorter term averages in the manner described in Section 3b. As can be seen in Table 1, the variance explained by $\mathbf{e}_1(z)$ decreases as the averaging period decreases.

The patterns of $\mathbf{e}_1(z_{500})$ and $\mathbf{e}_1(z_{1000})$ based on the shorter averaging periods (not shown) are almost

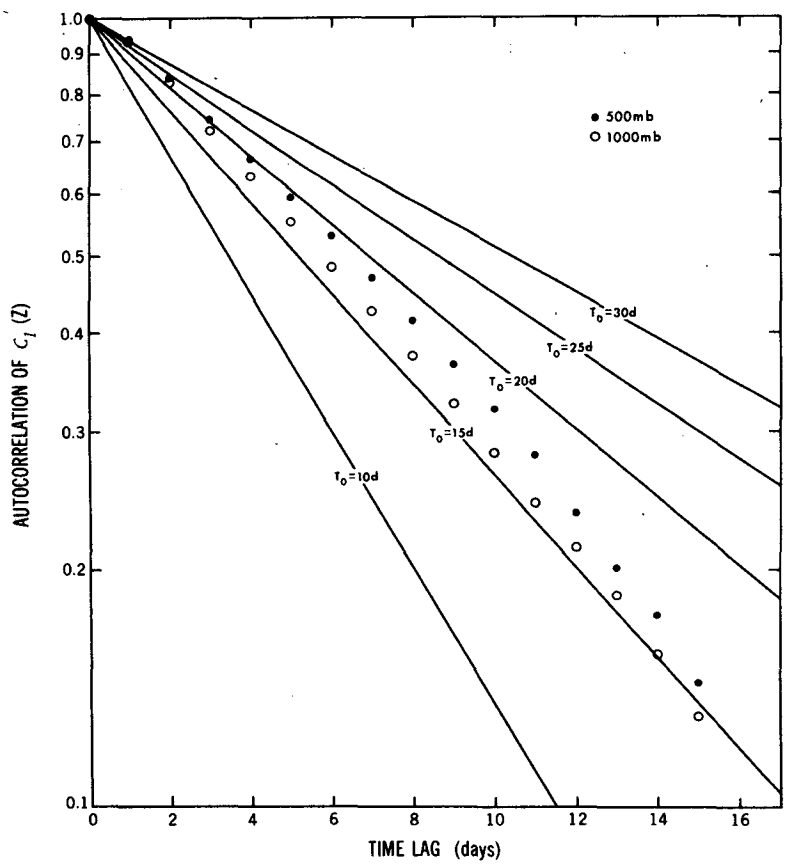

FIG. 20. Semi-logarithmic plot of lagged autocorrelation functions for the time series $C_1(z)$ based on daily data at 500 (solid dots) and 1000 (open circles) mb. The family of straight lines correspond to autocorrelation functions for first-order Markov processes with integral time scales T_0.

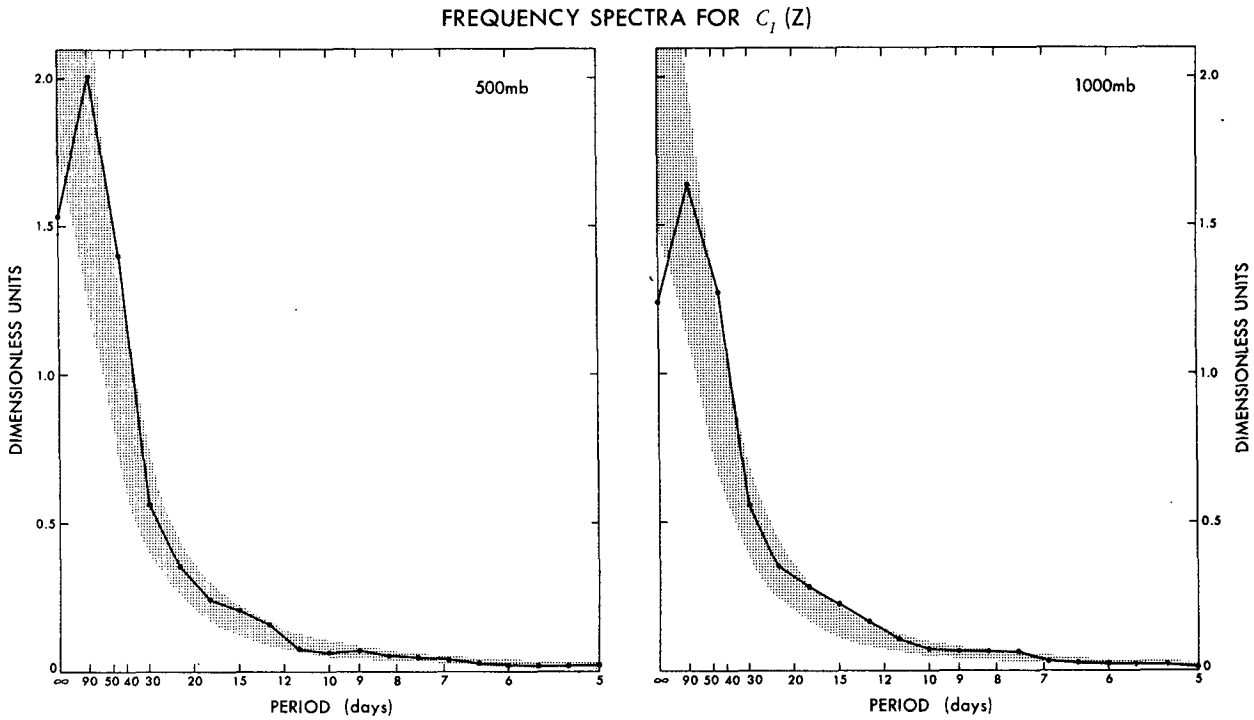

FIG. 21. Frequency spectra for the time series $C_1(z)$ based on daily data for 500 mb (left) and 1000 mb (right).

identical to those based on monthly means (shown in Figs. 5a and 7a). The spatial correlation coefficients between $e_1(z)$ based on monthly means and $e_1(z)$ based on *5-day means* are 0.99 and 0.98, for 500 and 1000 mb data, respectively. The correlation coefficients between $e_1(z)$ based on monthly means and $e_1(z)$ based on *daily data* are 0.97 and 0.95, for 500 and 1000 mb data, respectively. The strong correspondence between the spatial structure of the principal monthly and 5-day mean anomalies is also noted by H. Edmon and J. Horel (private communication) on the basis of NMC observational analyses.

As in the case for monthly mean data (Fig. 12 and Table 2), the coefficients $C_1(z)$ for 500 mb as determined using shorter averaging periods are strongly correlated with the corresponding coefficients for 1000 mb. The temporal correlations between $C_1(z_{500})$ and $C_1(z_{1000})$ is 0.89 for 5-day averages, and 0.83 for daily data.

The above results indicate that the spatial structure of the first eigenvector is remarkably insensitive to the averaging period of the input data. A measure of the persistence of this anomaly may be inferred from the characteristic time scale associated with the lagged autocorrelation function $r(\tau)$ of the coefficient $C_1(z)$. Here τ denotes the time lag. In Fig. 20 is presented a semi-logarithmic plot of $r(\tau)$ computed from $C_1(z)$ based on daily data of geopotential height at 500 (solid dots) and 1000 mb (open circles). The straight lines in the same diagram represent the autocorrelation function corresponding to first-order Markov processes with various decay time scales T_0, for which $r(\tau) = \exp - 2|\tau|/T_0$ (Leith, 1973). Here

$$T_0 = \int_{-\infty}^{\infty} r(\tau)d\tau \qquad (4)$$

and is hence a measure of the time span associated with an effectively independent sample in the time series of $C_1(z)$. It is seen from Fig. 20 that most of the data points for both pressure levels lie between the pair of straight lines with $T_0 = 15$ and 20 days. The autocorrelation time scale of $C_1(z)$ may also be estimated by computing the integral in (4) directly using the data displayed in Fig. 20. The values of T_0 thus obtained are 15.2 and 14.3 days for 500 and 1000 mb data, respectively. It is worth noting that this latter method is independent of any particular statistical model.

The frequency spectra of $C_1(z)$ derived from daily data are displayed in Fig. 21. The upper and lower bounds of the shaded envelopes in this figure represent the 95 and 5% confidence limits for a Markov red noise null continuum (Mitchell *et al.* 1966). These spectra are notable for their redness, with most of the power residing in the lowest resolvable frequency bands; and for the absence of significant spectral peaks. Rogers (1979, p. 131) has analyzed the coefficients associated with eigenvectors for daily observational data. His results indicate that the spectra of these coefficients are also characteristic of red noise.

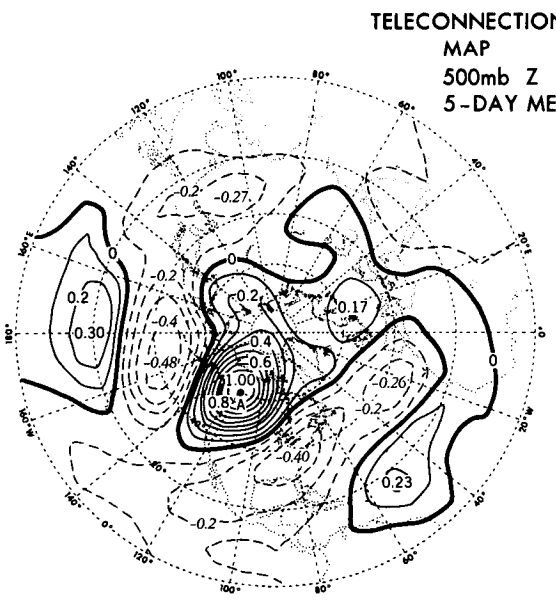

FIG. 22. Teleconnection map with reference point at 61°N, 120°W, based on model data for nonoverlapping 5-day averages of 500 mb height in winter. Note that the outermost circle in this map represents the equator.

In order to discern any lag relationship between the centers of action in $\mathbf{e}_1(z_{500})$, cross-correlation statistics with various temporal lags were computed using non-overlapping 5-day averages. In Fig. 22 is shown the wintertime distribution of the correlation coefficients between the 5-day mean fluctuations of 500 mb height at 61°N, 120°W (hereafter referred to as A) and the simultaneous values at other sites. This is hence a 1-point teleconnection pattern with zero lag (section 3e). In Fig. 23 is shown the corresponding charts with the fluctuations at A (a) leading by one 5-day period, and (b) lagging by one 5-day period. Note that the domain of analysis is extended to the equator in these charts. Point A is selected because it is located in the mid-point of an arc comprising the five anomaly centers mostly lying in the Western Hemisphere.

The teleconnection pattern based on 5-day means (Fig. 22) bears a strong resemblance to that based on monthly means (Fig. 6), and to the composite streamfunction chart $H(\psi) - L(\psi)$ (Fig. 14). Intercomparison between the patterns in Figs. 22 and 23 reveals that the fluctuations at the centers of action over the Pacific (20°N, 180°W and 43°N, 165°W) are better correlated/anticorrelated with the fluctuations at A when the latter lead by five days (Fig. 23a), than when they lag by five days (Fig. 23b). The absolute magnitudes of the values at the Pacific anomaly centers in Fig. 23a (with one lag) are actually as large as those in Fig. 22 (with zero lag). Conversely, the fluctuations at the Atlantic anomaly centers (20°N, 53°W and 43°N, 60°W) are better correlated/anticorrelated with the fluctuations at A when the latter lag by five days (Fig. 23b), than when they lead by five days (Fig. 23a). The cross-correlation coefficients hence exhibit a marked asymmetry with respect to the sign of temporal lag. This result is suggestive of a preferred west-to-east development of orderly wavetrains along a curved

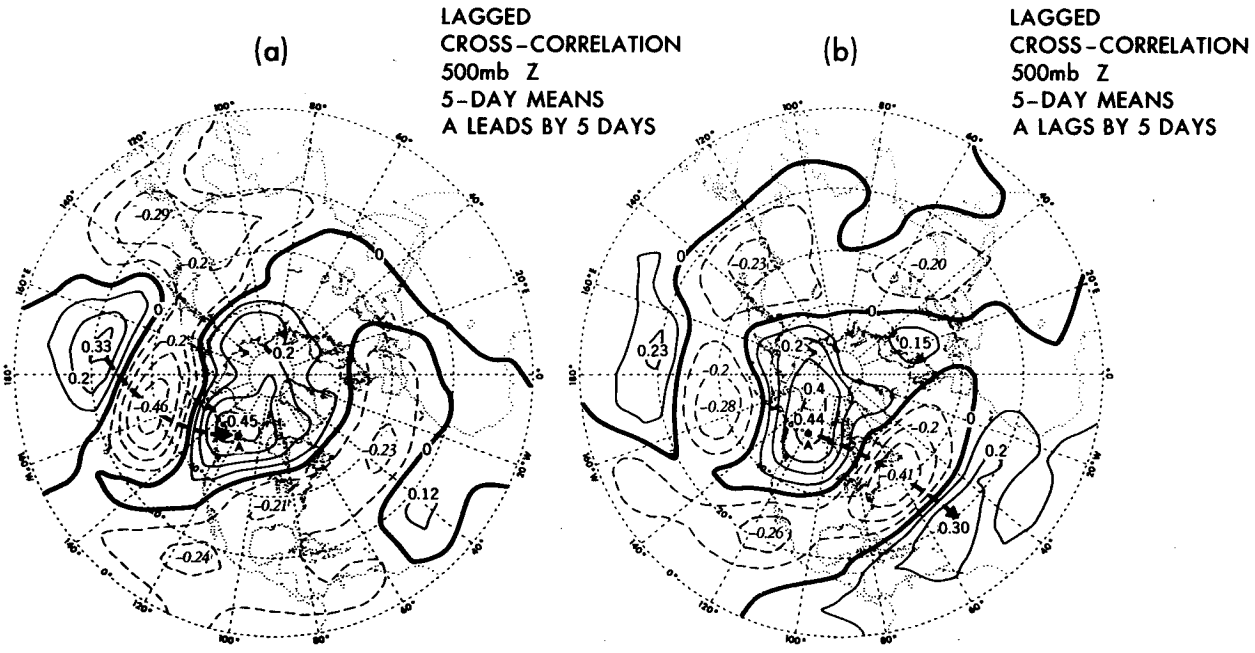

FIG. 23. Distributions of the correlation coefficients between non-overlapping 5-day averages of wintertime 500 mb height at reference point A (61°N, 120°W) and values elsewhere, for (a) fluctuations at A leading by one 5-day period, and (b) fluctuations at A lagging by one 5-day period. Note that the outermost circle in these maps represents the equator. The arrows with dashed shafts depict the curved path along which orderly wavetrains evolve.

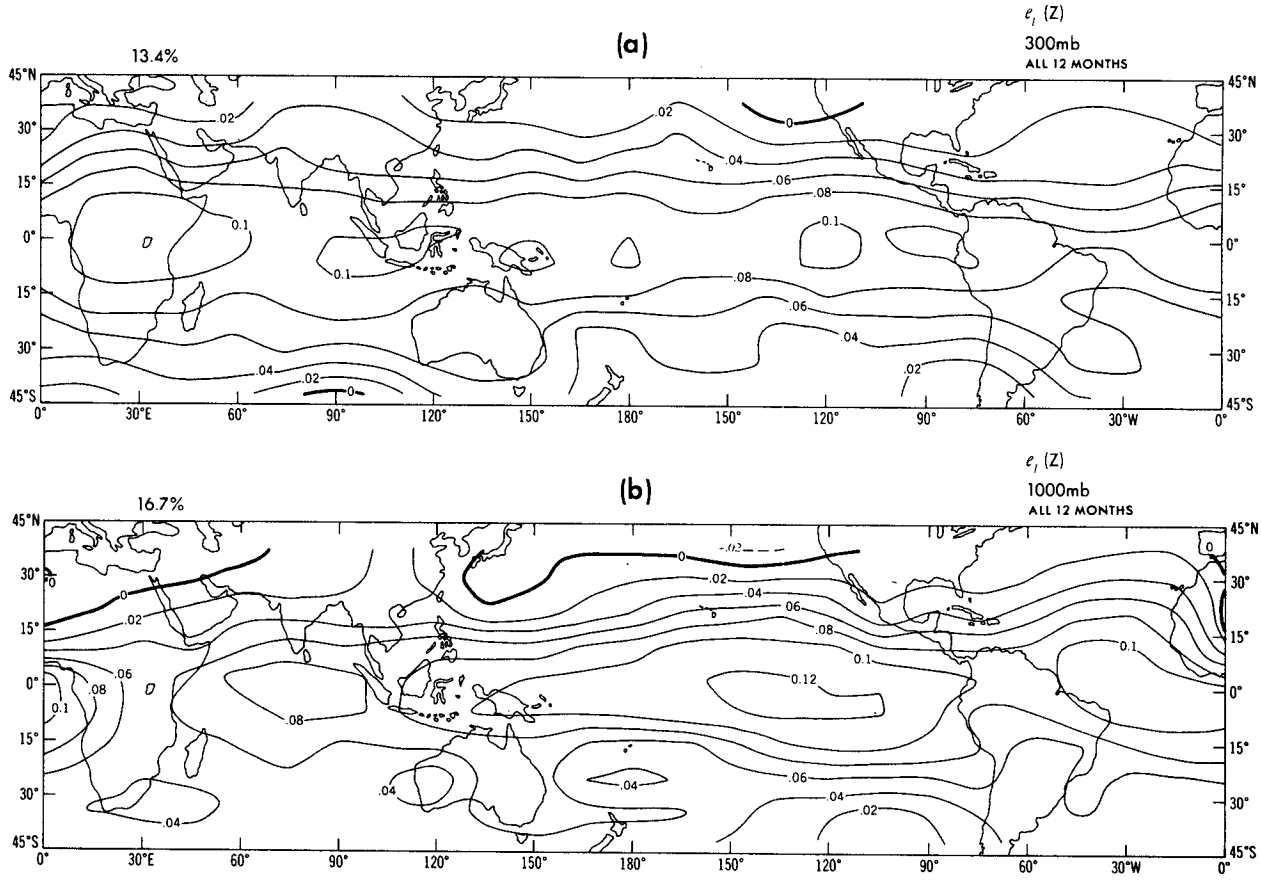

FIG. 24. Distributions of the eigenvectors associated with the first principal component of normalized monthly mean geopotential height at (a) 300 and (b) 1000 mb, for all 12 months of the year over the tropics.

path extending from the subtropical Pacific to the subtropical Atlantic (depicted by arrows with dashed shafts in Figs. 23a and 23b). Similar features have previously been identified by Hoskins *et al.* (1977) in numerical experiments with a linear barotropic model on a sphere. Cross-correlation statistics similar to those in Figs. 22 and 23 have been compiled by Edmon (1980) using NMC observational analyses. His results also indicate similar temporal evolution of teleconnection patterns.

8. Principal anomaly patterns for other regions and seasons

a. Tropics

In Fig. 24 are shown the distributions of $\mathbf{e}_1(z)$ associated with nonseasonal geopotential height fluctuations at (a) 300 and (b) 1000 mb over the tropics and subtropics. The eigenvector analysis is performed on a 240-point grid extending from 43°S to 38°N, with uniform latitude and longitude spacings of 9 and 15°, respectively. The input data consist of normalized monthly means for every month in the 15-year model integration. The eigenvectors at both pressure levels are noted for the lack of variation in the zonal direction. The normalized fluctuations associated with the first principal component attain maximum amplitudes with the same polarity over the entire equatorial zone. The strength of these fluctuations decreases monotonically on both sides of the equator. Such features are also evident in the patterns based on the months of December, January and February alone (not shown). The east–west sea level pressure seesaw associated with the Southern Oscillation, which has been extensively documented in the observational studies cited in Section 1, hence does not appear as a preferred mode of oscillation in the 15-year simulation. The next few eigenvectors for 1000 mb model data (not shown) also bear no resemblance to the anomaly pattern associated with the Southern Oscillation.

b. Northern Hemisphere summer

The distribution of $\mathbf{e}_1(z)$ using monthly means of 500 mb height for June, July and August in the 15-year simulation is shown in Fig. 25. The fraction of the total variance explained by this pattern is 9.8%, which is much smaller than the corresponding

value for winter (22.4%). It contains more small-scale features and bears no resemblance to its counterpart for the winter season (Fig. 5a). The summertime anomaly pattern having the closest correspondence to $\mathbf{e}_1(z)$ in winter is actually represented in the third eigenvector (not shown, variance explained: 7.3%), with most of the centers of action being shifted poleward by ~10° of latitude.

The rotated principal components based on summertime observational analyses are presented by Horel (1981, Fig. 5b). The centers of action in the first three observed eigenvectors are mostly located in the subtropics. The fourth eigenvector bears some resemblance to the Pacific/North American pattern observed in winter (Fig. 5b), with most of the centers of action being displaced north of their respective wintertime positions.

c. *Southern Hemisphere winter*

In Fig. 26 is shown the pattern of $\mathbf{e}_1(z)$ based on monthly mean values for June, July and August at 500 mb. This Southern Hemisphere eigenvector analysis is performed on a 112-point grid which is similar to that shown in Fig. 5a (solid dots). This eigenvector is characterized by a strong zonal symmetry, with the geopotential height field fluctuating with opposite signs about the 45°S latitude. The corresponding pattern of $\mathbf{e}_1(z)$ for the Southern Hemisphere summer (not shown) is similar to Fig. 26 and also exhibits little longitudinal dependence.

Trenberth (1980) has performed an eigenvector analysis of the 500 mb height in the Southern Hemisphere based on observational analyses pro-

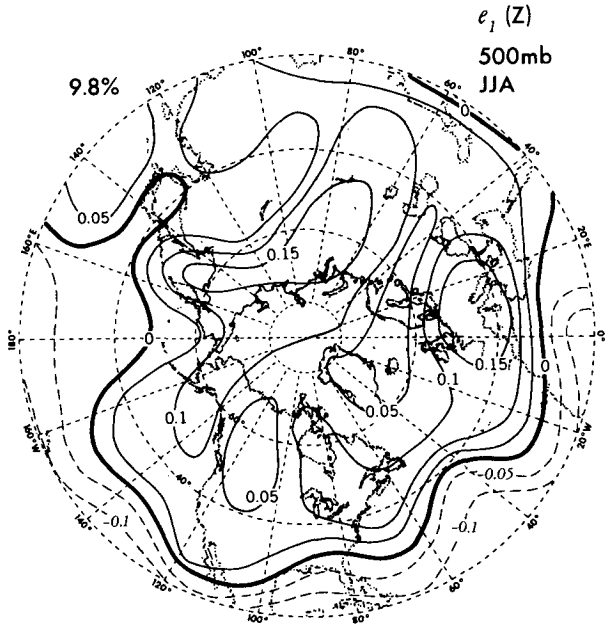

FIG. 25. As in Fig. 5a except for summer season.

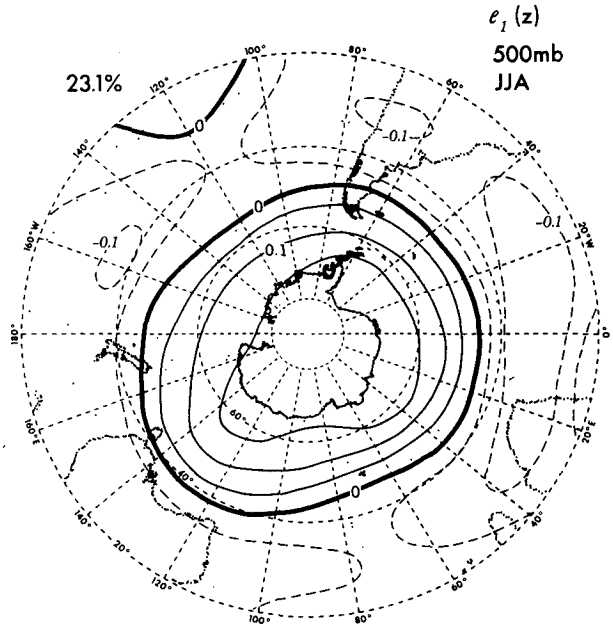

FIG. 26. As in Fig. 5a except for winter season in the Southern Hemisphere.

vided by the Australian Bureau of Meteorology. The first three observed eigenvectors were also found to be essentially zonal in character.

9. Summary and discussions

By analyzing a 15-year GCM simulation with no non-seasonal change in external forcing, we have identified the spatial and temporal characteristics of oscillatory phenomena generated internally in the model atmosphere. The wintertime standing oscillation which accounts for the largest fraction of the temporal variance in the Northern Hemisphere of the model is revealed by eigenvectors associated with the first principal components of selected variables (Figs. 5, 7, 9 and 11). These eigenvectors and the associated teleconnection charts indicate that the most preferred mode of oscillation has a coherent three-dimensional structure, which is similar to that associated with the most prevalent anomaly complex observed in the atmosphere. In the middle and upper troposphere, the preferred southwest-to-northeast tilt of the elongated vortices in the anomaly pattern (Fig. 14), as well as the transient evolution of the 5-day mean charts (Fig. 23) are similar to those associated with developing Rossby wavetrains on a sphere (Hoskins *et al.*, 1977).

The behavior of synoptic-scale transient disturbances and hydrological processes in the model during the outstanding anomaly episodes are studied by composite charts. These features, together with the concomitant large-scale circulation patterns, constitute an internally consistent set of meteoro-

logical phenomena which are in conformity with the dynamics and physics prescribed in the model, and with the synoptic climatology of the observed atmosphere.

The same anomaly pattern shows up clearly in analyses of model data with averaging periods ranging from one day to one month. The persistence time scale associated with this anomaly pattern is estimated to be approximately 15 days (Fig. 20), which is considerably longer than the corresponding value deduced from the time series for single grid points. The latter quantity, as determined by Manabe and Hahn (1981, Fig. 5.12) using similar techniques described here, is on the order of five days. In view of the well-defined spatial pattern as well as the strong temporal autocorrelation of the first principal component, it is unlikely that this particular anomaly arises out of inadequate sampling of less organized daily weather fluctuations as discussed in Leith (1973) and Madden (1976). The long memory inherent in the first principal component accounts for the redness of its frequency spectra (Fig. 21). The absence of any distinct spectral peaks indicates that this anomaly pattern does not occur in regular cycles.

The spatial structure of the most prominent anomaly pattern is seen to be dependent on the season and the areal domain of investigation. The most dominant standing mode in the tropics at both 1000 and 300 mb (Fig. 24) exhibits a weak longitudinal dependence. The maximum amplitudes occur along an elongated band centered at the equator. The first eigenvector in the Northern Hemisphere for the summer season (Fig. 25) contains much more small-scale features than its counterpart for winter. The principal anomaly pattern in the Southern Hemisphere (Fig. 26) is noted for its zonal symmetry.

The appearance in this "unperturbed" model of extratropical anomaly patterns which are not unlike those actually observed in the atmosphere suggests that the latter might occur in the absence of non-seasonal perturbations to the natural climate system. However, the body of evidence presented in this study certainly does not rule out the possibility that external perturbations such as changes in sea surface temperature, cloudiness and ground hydrology might be responsible for enhancement in the frequency of occurrence and/or intensity of these anomalies. Moreover, the discrepancies between model and observations with respect to the exact details of the anomaly structure could in part be accounted for by the presence of external changes in the real atmosphere. The fact that only a subset of the family of observed anomaly patterns (such as those documented by Wallace and Gutzler, 1981) is discernible in the model simulation further hints at the potential role of external forcing in the onset and maintenance of the remaining patterns.

The absence of the Southern Oscillation in the model tropics as well as the general lack of significant teleconnections between the tropics and the extratropics in the model are indicative of the central role of non-seasonal sea surface temperature anomalies and related processes in the variability of the tropical atmosphere. Since such processes are not incorporated in the present version of the GCM, it is not surprising that both the amplitude (Manabe and Hahn, 1981, Fig. 5.10) and pattern (Fig. 24b) of tropical anomalies in the simulation are not realistic. On the other hand, the sensitivity experiments analyzed by Rowntree (1972, 1976a,b) and Kutzbach *et al.* (1977) have demonstrated that both the tropical and extratropical circulations in model atmospheres do respond strongly to sea surface temperature anomalies. These studies suggest that a coupled ocean–atmosphere model with the necessary dynamical and physical feedback mechanisms is needed for scrutinizing the full range of phenomena associated with atmospheric and oceanic variability.

Acknowledgments. I would like to thank Dr. S. Manabe, Dr. A. H. Oort and other staff members of GFDL for their encouragement and support throughout the course of this work, and for offering constructive comments on earlier versions of the manuscript. I am indebted to Professor John M. Wallace, Mr. David S. Gutzler and their associates at the University of Washington for many stimulating discussions on some of the results. The figures were drafted by the Scientific Illustration Group at GFDL. The manuscript was typed by Ms. Dawn M. Eldridge. I am supported at the Geophysical Fluid Dynamics Program, Princeton University, by NOAA Grant 04-7-022-44017.

APPENDIX

Eigenvector Analysis of Observational Data

The model results in Fig. 12 and Table 2 indicate that the time series of the coefficients $\mathbf{C}_1(z_{500})$, $\mathbf{C}_1(T_{850})$ and $\mathbf{C}_1(z_{1000})$, as determined individually for each variable, are strongly correlated with each other, and with the time series determined by a combined three-variable eigenvector representation [i.e., $\mathbf{C}_1(z_{500}, T_{850}, z_{1000})$]. On the other hand, single-variable eigenvector analyses of the observational NMC analyses indicate that the coefficients associated with the first principal components [i.e., $\mathbf{C}_1(z_{500})$, $\mathbf{C}_1(T_{850})$ and $\mathbf{C}_1(z_{1000})$] do not exhibit such strong correlations. For instance, it was found that the first principal component of the observed 850 mb temperature field is related to the *second* (instead of the first) principal component of the observed 500 mb height. In order to make a meaningful comparison of the model results with observations, one would hence have to select those observed eigen-

vectors $\mathbf{e}_{k_1}(z_{500})$, $\mathbf{e}_{k_2}(T_{850})$ and $\mathbf{e}_{k_3}(z_{1000})$ such that the associated coefficients $\mathbf{C}_{k_1}(z_{500})$, $\mathbf{C}_{k_2}(T_{850})$ and $\mathbf{C}_{k_3}(z_{1000})$ are strongly correlated with each other. This search procedure may be circumvented by performing a combined eigenvector representation of all three observed variables, since each principal component in this combined representation offers a collective description of the temporal variation of three spatial patterns, one for each variable.

The observed patterns presented in Figs. 5b, 7b and 9b correspond to the first eigenvector $\mathbf{e}_1(z_{500}, T_{850}, z_{1000})$ of the combined three-variable representation. The eigenvector analysis was performed on a 111-point grid which is similar to that depicted in Fig. 5a. The 850 mb temperature for nine grid points situated in regions of high terrain were not included in the analysis. All input data were normalized by the local standard deviation. Hence $\mathbf{R}(z_{500}, T_{850}, z_{1000})$ defined in (1) is a 324×324 correlation coefficient matrix. The first eigenvector of this matrix explains 13.7% of the total variance. For a more compatible comparison with model results, which are based on single-variable eigenvector representations, the observed eigenvectors were scaled such that $\mathbf{e}_k(z_{500}, T_{850}, z_{1000})\ \mathbf{e}_k^{\mathrm{T}}(z^{500}, T_{850}, z_{1000}) = 3$.

The observed eigenvector patterns as determined by the combined three-variable representation exhibit strong resemblance to those presented in other observational studies based on single-variable representations. For instance, Fig. 5b is similar to the second eigenvector for 500 mb height (Wallace and Gutzler, 1981, Fig. 27); Fig. 7b is similar to the first eigenvector for sea level pressure (Wallace and Gutzler, 1981, Fig. 11); and Fig. 9b is similar to the first eigenvector for sea level temperature (Barnett, 1978, Fig. 3).

For the model data, the first eigenvector as determined using the combined three-variable representation is almost identical to the first eigenvectors based on single-variable representations (see beginning of Section 6 for further details). Hence, one would reach the same conclusions when the model patterns as determined by either method are compared with the observed eigenvector patterns, which are based on a combined three-variable representation. We have chosen to present the model patterns based on single-variable eigenvector representations in anticipation of the discussion on eigenvectors for 5-day averages and daily data (Section 7), which are also based on single-variable representations.

REFERENCES

Barnett, T. P., 1978: Estimating variability of surface air temperature in the Northern Hemisphere. *Mon. Wea. Rev.*, **106**, 1353–1367.

Bjerknes, J., 1966: A possible response of the atmospheric Hadley circulation to equatorial anomalies of ocean temperature. *Tellus*, **18**, 820–829.

——, 1969: Atmospheric teleconnections from the equatorial Pacific. *Mon. Wea. Rev.*, **97**, 162–172.

Blackmon, M. L., 1976: A climatological spectral study of the 500 mb geopotential height of the Northern Hemisphere. *J. Atmos. Sci.*, **33**, 1607–1623.

——, and N-C. Lau, 1980: Regional characteristics of the Northern Hemisphere wintertime circulation: A comparison of the simulation of a GFDL general circulation model with observations. *J. Atmos. Sci.*, **37**, 497–514.

——, J. M. Wallace, N-C. Lau and S. L. Mullen, 1977: An observational study of the Northern Hemisphere wintertime circulation. *J. Atmos. Sci.*, **34**, 1040–1053.

——, R. A. Madden, J. M. Wallace and D. S. Gutzler, 1979: Geographical variations in the vertical structure of geopotential height fluctuations. *J. Atmos. Sci.*, **36**, 2450–2466.

Charney, J. G., and J. G. DeVore, 1979: Multiple flow equilibria in the atmosphere and blocking. *J. Atmos. Sci.*, **36**, 1205–1216.

Chervin, R. M., J. E. Kutzbach, D. D. Houghton and R. G. Gallimore, 1980: Response of the NCAR general circulation model to prescribed changes in ocean surface temperature. Part II: Midlatitude and subtropical changes. *J. Atmos. Sci.*, **37**, 308–332.

Dickson, R. R., and J. Namias, 1976: North American influences on the circulation and climate of the North Atlantic sector. *Mon. Wea. Rev.*, **104**, 1255–1265.

Edmon, H. J., 1980: Time evolution of teleconnection patterns. *Proc. Fifth Annual Climate Diagnostics Workshop*, Seattle, Climate Analysis Center, Washington DC 20233, 85–92.

Gill, A. E., 1980: Some simple solutions for heat-induced tropical circulations. *Quart. J. Roy. Meteor. Soc.*, **106**, 447–462.

Gordon, C. T., and W. F. Stern, 1974: Spectral Modelling at GFDL. The GARP Programme on Numerical Experimentation—Report of the International Symposium on Spectral methods in numerical weather prediction. Copenhagen, Rep. No. 7, pp. 46–82. [Available from Secretariat of the WMO].

Hardy, D. M., and J. J. Walton, 1978: Principal components analysis of vector wind measurements. *J. Appl. Meteor.*, **17**, 1153–1162.

Horel, J. D., 1981: A rotated principal component analysis of the interannual variability of the Northern Hemisphere 500 mb height field. *Mon. Wea. Rev.*, **109**, 2080–2092.

——, and J. M. Wallace, 1981: Planetary scale atmospheric phenomena associated with the Southern Oscillation. *Mon. Wea. Rev.*, **109**, 813–829.

Hoskins, B. J., and D. J. Karoly, 1981: The steady linear response of a spherical atmosphere to thermal and orographic forcing. *J. Atmos. Sci.*, **38**, 1179–1196.

——, A. J. Simmons and D. G. Andrews, 1977: Energy dispersion in a barotropic atmosphere. *Quart. J. Roy. Meteor. Soc.*, **103**, 553–567.

Julian, P. R., and R. M. Chervin, 1978: A study of the Southern Oscillation and Walker Circulation phenomenon. *Mon. Wea. Rev.*, **106**, 1433–1451.

Kidson, J. W., 1975: Tropical eigenvector analysis and the Southern Oscillation. *Mon. Wea. Rev.*, **103**, 187–196.

Kutzbach, J. E., 1967: Empirical eigenvectors of sea-level pressure, surface temperature and precipitation complexes over North America. *J. Appl. Meteor.*, **6**, 791–802.

——, 1970: Large-scale features of monthly mean Northern Hemisphere anomaly maps of sea-level pressure. *Mon. Wea. Rev.*, **98**, 708–716.

——, R. M. Chervin and D. D. Houghton, 1977: Response of the NCAR general circulation model to prescribed changes in ocean surface temperature. Part 1: Mid-latitude changes. *J. Atmos. Sci.*, **34**, 1200–1213.

Leith, C. E., 1973: The standard error of time-averaged estimates of climatic means. *J. Appl. Meteor.*, **12**, 1066–1069.

Madden, R. A., 1976: Estimates of the natural variability of time-averaged sea-level pressure. *Mon. Wea. Rev.*, **104**, 942–952.

Manabe, S., 1969: Climate and the ocean circulation. I. The atmospheric circulation and the hydrology of the earth's surface. *Mon. Wea. Rev.*, **97**, 739–774.

——, and D. G. Hahn, 1981: Simulation of atmospheric variability. *Mon. Wea. Rev.*, **109**, 2260–2286.

——, ——, and J. L. Holloway, Jr., 1979: Climate simulations with GFDL spectral models of the atmosphere: Effects of spectral truncation. *GARP Publ. Ser.* No. 22, Vol. 1, Secretariat of the World Meteorological Organization, 41–94. [NTIS N8027917].

Mitchell, J. M., B. Dzerdzeevskii, H. Flohn, W. L. Hormeyr, H. H. Lamb, K. N. Rao and C. C. Wallen, 1966: Climate change. WMO Tech. Note, 79, WMO No. 195, TP100, Secretariat of the World Meteorological Organization, 79 pp.

Namias, J., 1969: Seasonal interactions between the North Pacific Ocean and the atmosphere during the 1960's. *Mon. Wea. Rev.*, **97**, 173–192.

——, 1976: Some statistical and synoptic characteristics associated with El Nino. *J. Phys. Oceanogr.*, **6**, 130–138.

NCAR, 1978: NCAR Software Library, Vol. 1. NCAR Tech. Note TN/IA-105. Available from NCAR Publications Office, Boulder, CO 80307.

O'Connor, J. F., 1969: Hemispheric teleconnections of mean circulation anomalies at 700 mb. ESSA Tech. Rep. WB-10, U.S. Weather Bureau. Superintendent of Documents, U.S. Govt. Printing Office, Washington, DC 20402. [NTIS N69-34858].

Opsteegh, J. D., and H. M. van den Dool, 1980: Seasonal differences in the stationary response of a linearized primitive equation model: Prospects for long-range weather forecasting? *J. Atmos. Sci.*, **37**, 2169–2185.

Rogers, J. C., 1979: The North Pacific Oscillation and eigenvectors of Northern Hemisphere atmospheric circulation during winter. NCAR Cooperative thesis No. 56, 177 pp. Available from NCAR Publications Office, Boulder, Colorado 80307. [ISSN 004-6145].

——, and H. van Loon, 1979: The seesaw in winter temperatures between Greenland and Northern Europe. Part II: Some oceanic and atmospheric effects in middle and higher latitudes. *Mon. Wea. Rev.*, **107**, 509–519.

Rowntree, P. R., 1972: The influence of tropical east Pacific Ocean temperatures on the atmosphere. *Quart. J. Roy. Meteor. Soc.*, **98**, 290–321.

——, 1976a: Tropical forcing of atmospheric motions in a numerical model. *Quart. J. Roy. Meteor. Soc.*, **102**, 583–606.

——, 1976b: Response of the atmosphere to a tropical Atlantic ocean temperature anomaly. *Quart. J. Roy. Meteor. Soc.*, **102**, 607–626.

Stefanick, M., 1981: Space and time scales of atmospheric variability. *J. Atmos. Sci.*, **38**, 988–1002.

Trenberth, K. E., 1980: Atmospheric quasi-biennial oscillations. *Mon. Wea. Rev.*, **108**, 1370–1377.

van Loon, H., and J. C. Rogers, 1978: The seesaw in winter temperatures between Greenland and Northern Europe. Part I: General description. *Mon. Wea. Rev.*, **106**, 296–310.

Walker, G. T., and E. W. Bliss, 1932: World Weather V. *Mem. Roy. Meteor. Soc.*, **4**, 53–84.

Wallace, J. M., and D. S. Gutzler, 1981: Teleconnections in the geopotential height field during the Northern Hemisphere winter. *Mon. Wea. Rev.*, **109**, 784–812.

Webster, P. J., 1972: Response of the tropical atmosphere to local, steady, forcing. *Mon. Wea. Rev.*, **100**, 518–540.

——, 1981: Mechanisms determining the atmospheric response to sea surface temperature anomalies. *J. Atmos. Sci.*, **38**, 554–571.

Wright, P. B., 1977: The Southern Oscillation patterns and mechanisms of teleconnections and persistence. Hawaii Inst. Geophys. Rep. HIG-77-13. University of Hawaii, 107 pp.